METAL OXIDE NEGATIVE ELECTRODES FOR SODIUM-ION BATTERIES

by

Zachary Brown

Submitted in partial fulfilment of the requirements
for the degree of Master of Science

at

Dalhousie University
Halifax, Nova Scotia
July 2015

DEDICATION PAGE

I dedicate this thesis to my immediate family. My brother, Adam Brown, who has taught me that no matter what “it’s all good”. My parents, Les and Alex Brown, have taught me the most valuable lesson, to pursue what I enjoy. This advice has lead me to pursue a career in science.

TABLE OF CONTENTS

LIST OF TABLES

LIST OF FIGURES

ABSTRACT

Sodium-ion battery technology is of interest for energy storage applications because it has the potential to be sustainable and cost effective. Currently, the lack of a suitable negative electrode material limits the commercialization of sodium-ion batteries. In this work, metal oxides were explored as negative electrode candidates for sodium-ion batteries. Using electrochemical measurements, powder X-ray diffraction and Mössbauer spectroscopy, the electrochemistry and structure of metal oxides were investigated. Mixed transition metal titanate and vanadate materials that operated at low voltage with high volumetric capacity were synthesized, and observed to undergo unique sodiation mechanisms. The electrochemistry of binary metal oxides was also explored at elevated temperatures, leading to the activation of materials with sodium that are usually inactive at room temperature. Overall, the materials studied show promise in terms of achieving high energy density but more detailed investigations need to be performed in order to evaluate their commercial potential.

LIST OF SYMBOLS AND ABBREVIATIONS USED

$\overline{E_D}$	Mean Doppler-Effect Energy
$\overline{E_k}$	Mean Thermal Kinetic Energy
μ_N	Nuclear Bohr Magneton
E_D	Doppler-Effect Energy
E_Q	Quadrupole Energy
E_R	Recoil Energy
E_{cell}	Cell Potential
E_e	Energy of Excited State
E_g	Energy of Ground State
E_m	Zeeman Effect Energy
E_{tot}	Total Energy Above Ground State
E_γ	Energy of Emitted γ-ray Photon
I_0	Intensity of Incident Radiation
I_Z	Spin Quantum State
Q_c	Capacity Upon Charge
Q_d	Capacity Upon Discharge
V_x	Initial Velocity
$f_n(\Theta)$	Atomic Scattering Factor
m_I	Magnetic Quantum Number
n_e	Number of Electrons
v_s	Velocity of Source
x_n, y_n, z_n	Fractional Atomic Coordinates
$\Psi_s(0)_A$	Non-Relativistic Schrödinger Wavefunction at $r = 0$ For The Source
$\Psi_s(0)_B$	Non-Relativistic Schrödinger Wavefunction at $r = 0$ For The Absorber
$\mu_{negative}$	Negative Electrode Chemical Potential
$\mu_{positive}$	Positive Electrode Chemical Potential
BMF	Blown Microfiber
EV	Electric Vehicle
$\hbar$	Reduced Planck Constant
h, k, l	Miller Indicies
HHI	Herfindahl-Hirschman index
$\mathrm{H_m}$	Zeeman Splitting
PI	Polyimide
PVDF	Polyvinylidene Fluoride
SC	Super C Carbon Black
SEI	Solid Electrolyte Interphase
SP	Super P Carbon Black
XRD	X-ray diffraction
Γ	Full Width Half Maximum Mössbauer Spectrum Peak
Δ	Quadrupole Splitting
B	Full Width at Half Maximum XRD Pattern Peak
C	Theoretical Capacity

CE	Coulombic Efficiency
$DW(hkl)$	Debye-Waller Factor
E	Energy of Nuclear Transition
F	Faraday's Constant
$F(hkl)$	Geometrical Structure Factor
H	Magnetic Field Flux Density
I	Angular Momentum Quantum Number
$I(\theta)$	Total Reflected Intensity
K	Constant
$L(\theta)$	Lorentz Factor
M	Mass of Nucleus
M_m	Molar Mass
$M(hkl)$	Multiplicity Factor
$P(\theta)$	Polarization Factor
Q	Nuclear Quadrupole Moment
c	Velocity of Light
d	Bragg Spacing
e	Electronic Charge
eq	Maxium Value of The Electric Field Gradient
f	Recoil Fraction
g	Nuclear g-Factor
n	Integer Indicating Order of Reflection
t	Average Dimension of Crystallite
v	Velocity Change Due to Recoil
θ	Angle Between Incident X-rays and Diffracting Planes
δ	Isomer Shift
δE	Difference Between Energy of Nuclear Transition and Energy Emitted γ-ray Photon
λ	Wavelength of Incident X-rays
ω	Photon Angular Frequency

ACKNOWLEDGEMENTS

I would like to acknowledge my supervisor, Dr. Mark Obrovac. I have a significant amount of travel experience related to both academia and industry because of him. His patience with my exploration of my own ideas and making mistakes is greatly appreciated. I feel I have gained invaluable knowledge during my time under his supervision and am very thankful for that. Of course, this work would not be possible without financial support from the NSERC CREATE DREAMS (Dalhousie Research in Energy, Advanced Materials and Sustainability) program.

My supervisory committee members have also have been a large part of my academic studies as well, even though they may not know it. Dr. Jeff Dahn has taught me never to trust anything I read and that I can find “hoo-hah” even in peer-reviewed journals. Also his ability to communicate ideas in a simple matter is always impressive and I have tried to adopt similar approaches. Dr. Mary Anne White was the first person to introduce me to Materials Science in an exciting manner; I will be forever grateful for that. Further, her leadership in the DREAMS program has given me experiences unique to any graduate degree.

I also would like to acknowledge the significant contribution Stephanie Smith made to work from Chapter 3 as a DREAMS undergraduate summer student. With her hard work we were able to explore many materials.

The folks at 3M, notably Dr. Zhonghua Lu, Dr. Kevin Eberman and Dr. Vincent Chevrier, really have opened my eyes to applying science in industry. I cannot stress enough how much I learned from their expertise in both industry and life.

The colleagues that have become friends should be acknowledged as I have learned a great deal from them as well. In no particular order these are: Ryan F., Douglas, Kalani, Xiuyun, Lauren, Zilai, John T., Zhijia, Lituo, Leyi, Leah, Jim, Stephen, Andrew, Chris, John C., John N., Nick, Preston, Ryan S., Jan, Connor, Alex and the many summer students of the Obrovac lab. Dr. Tim Hatchard has also helped me considerably with constructing experimental setups around the lab and has participated in fulfilling discussions. I have had a lot of fun with everyone during my Master’s studies at Dalhousie.

Close friends from home that distract me my work are also immensely helpful, helping me clear my mind and approach problems with a fresh perspective. These friends include Max, Darcy, Logan, James, Jory, Andrew, Ben, Matt and Barret.

Finally my parents support, ranging from providing home cooked meals to figuring out my future goals, has gotten me through hectic times during my studies and I cannot thank them enough for that.

CHAPTER 1 INTRODUCTION

1.1 MOTIVATION

It has been shown that the future climate in Canada over the next century will involve a significant increase in surface temperature even with an immediate reduction in carbon emissions.[1] Unfortunately the scenario may be even worse than predicted, since Canada is still behind in reducing carbon emissions, with the acknowledgement that Canada will not achieve its Copenhagen Accord target of reducing Greenhouse Gas (GHG) emissions by 17% in 2020 (relative to 2005).[2] Figure 1.1 shows that road transportation accounted for the second largest sector of GHG emissions in Canada, responsible for 19% in 2012, just behind oil and gas which contributed 25% of GHG emissions.[1,3] The majority of this road transportation consists of fossil-fuelled trucks and automobiles.[1] Therefore, commercialization of electric vehicles (EVs) for the average consumer can have a large impact in reducing GHG emissions in Canada. Although in certain cases the total cost of ownership of today's EVs can be less expensive compared to fossil-fuelled vehicles,[4] the expensive upfront cost still discourages the average consumer from purchasing an EV. Even though there are efforts to emphasize the lower total cost of ownership to the consumer,[5] ideally the upfront cost needs to be decreased in order to achieve a national, as well as global, transition from fossil-fuelled vehicles to EVs.

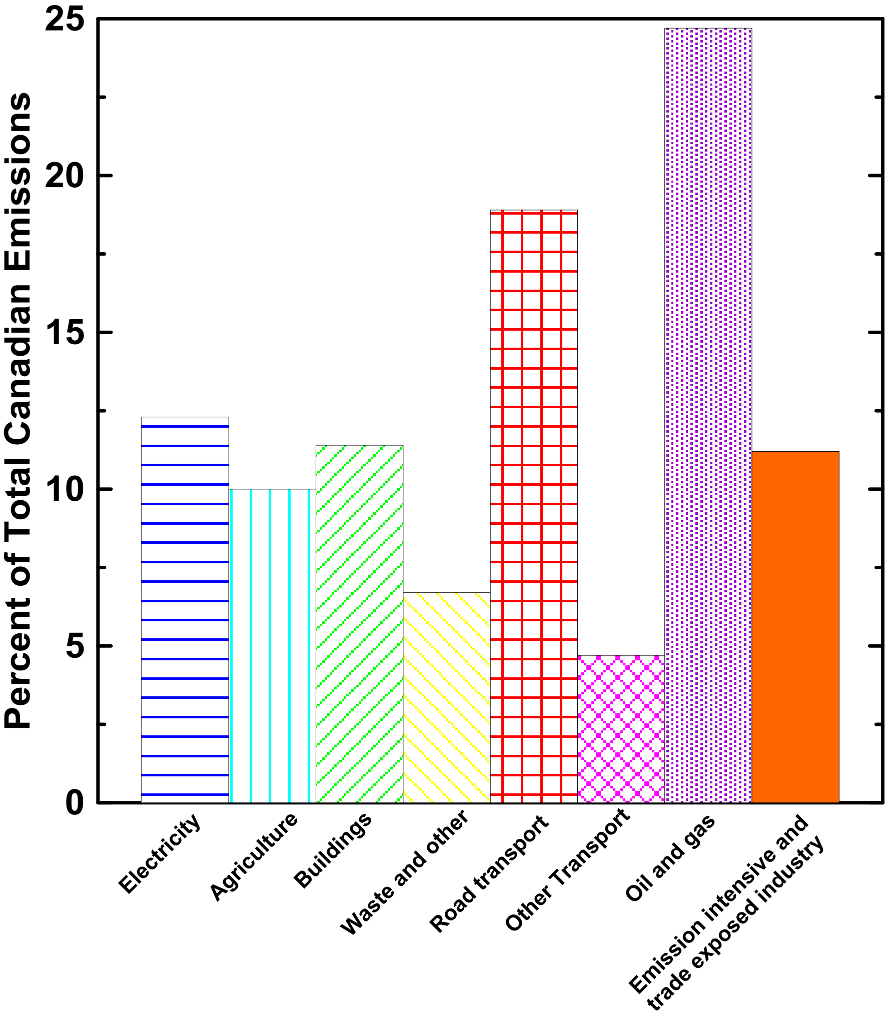

Figure 1.1 GHG emissions by sector in 2012 as a percent of total Canadian emissions. Data from reference 1.

Currently, lithium-ion batteries are the leading energy storage technology used in electric vehicles.[6,7] These battery packs are also one of the most costly components of an EV, but that cost is decreasing, for example battery packs in the Tesla Model S can be less than 300 \$ kWh^{-1}.[8] Further, the US Department of Energy defined a driving range target value of 300 miles in order to achieve mass market penetration of EVs.[9] The specific power and energy density of lithium-ion batteries need to each approximately double in order to reach this target with current automobile designs.[6] Due to the difficult task of reducing cost while improving performance for lithium-ion batteries, it is worth pursuing alternative battery technologies.

Figure 1.2 shows a plot of the crustal scarcity as well as the calculated Herfindahl-Hirschman Index (HHI) for elemental production (HHI_p) and elemental reserves (HHI_r) for lithium and sodium. The HHI is a financial tool commonly used to measure the monopoly of entities over a commodity or product, where a large HHI is characteristic of a highly concentrated market for the product and a small HHI is characteristic of a diffuse market for the product.[10] The U. S. Department of Justice and the Federal Trade Commission have designated markets as unconcentrated when HHI < 1500, moderately concentrated when the HHI is 1500-2500, and highly concentrated when HHI>2500.[11]

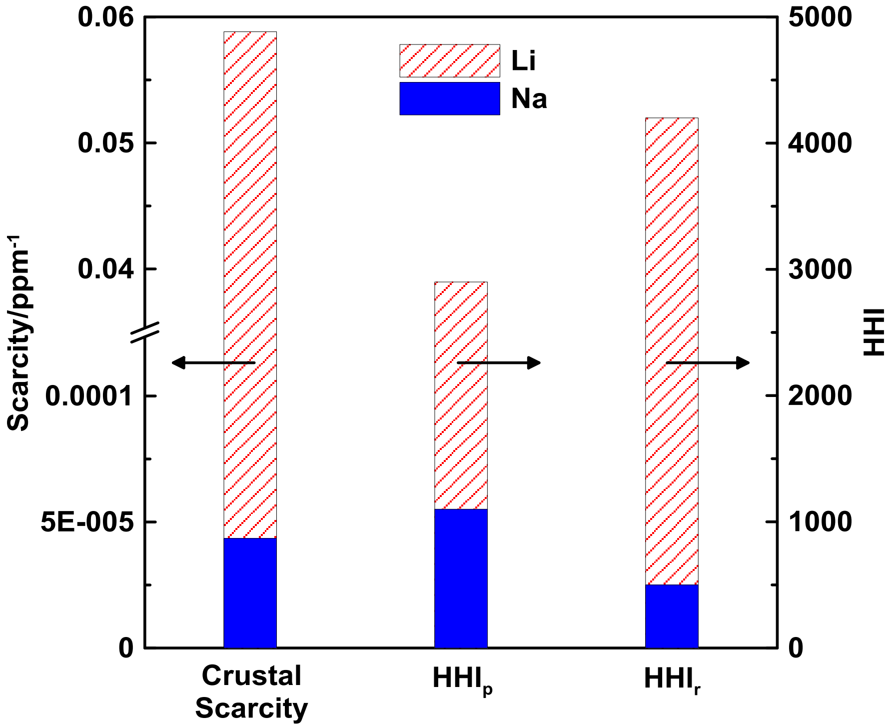

Figure 1.2 Crustal scarcity, HHI for elemental production (HHI_p), and HHI for elemental reserves (HHI_r) of lithium and sodium. Data from reference 12.

The HHI_p reflects the geopolitics of the element and the HHI_r reflects the distribution of reserves in the earth's crust. The scarcity (i. e. the inverse of crustal abundance) accounts for the weight fraction of elements and their crustal abundance. As shown in Figure 1.2, the scarcity of lithium is three orders of magnitude larger than sodium. Further, both the HHI_p and HHI_r are highly concentrated for lithium whereas the HHI_p and HHI_r are not concentrated for sodium. Also, lithium electrochemically alloys with aluminum at low voltages whereas sodium does not.[13] Therefore, an immediate benefit of sodium-ion batteries is the ability to use the cost effective aluminum current collector for both positive and negative electrodes.[14] Finally, the larger ionic radius of Na^+ (1.02 Å) compared to Li^+ (0.76 Å) (for a coordination number of six) can lead to a more diverse chemistry with sodium.[15] For example, the formation of layered structures with first row transition metal ions in oxides is more favorable with sodium compared to lithium.[15] This can provide more opportunities to develop low cost electrode materials by substituting cheaper and more sustainable transition metal ions in the layered structures. With these potential benefits, pursuing research in analogous sodium-ion battery technology might lead to battery pack cost reduction, and also might provide a more sustainable alternative to lithium-ion battery technology.[16,17] The lack of a negative electrode of suitable energy density is an important factor limiting sodium-ion batteries from being commercialized.[14] The purpose of this thesis work is to explore negative electrode materials suitable for sodium-ion batteries.

1.2 BACKGROUND

1.2.1 Lithium-Ion and Sodium-Ion Batteries

It is worth discussing the basic principles of how a lithium-ion battery operates[18] because these principles are directly analogous to the operation of sodium-ion battery. A schematic diagram of a lithium-ion battery is shown in Figure 1.3. The basic components consist of a positive electrode, separator, and negative electrode, all soaked with electrolyte. The cell voltage of a metal-ion cell is the potential difference between the positive and negative electrode materials as given by:

$$E_{cell} = \frac{-(\mu_{positive} - \mu_{negative})}{n_e e} \tag{1.1}$$

where E_{cell} is the cell potential measured in volts, $\mu_{positive}$ and $\mu_{negative}$ are the chemical potentials of the positive and negative electrode, respectively, with respect to lithium in units of electron volts, n_e is the number of electrons transferred in the chemical reaction, and e is electronic charge. In most commercial lithium-ion cells, the positive and negative electrode typically consist of a layered transition metal oxide ($LiMO_2$) and graphite, respectively. These electrode materials are coated onto current collectors in order to enhance electron conductivity. As described above, lithium alloys with aluminum at low voltage, so copper is typically used for the negative electrode current collector. The separator is typically made of both high purity polyethylene and polypropylene where the polyethylene layer is sandwiched in between two polypropylene layers. Ion conducting electrolytes typically comprise of a lithium salt dissolved in an aprotic organic carbonate solvent.

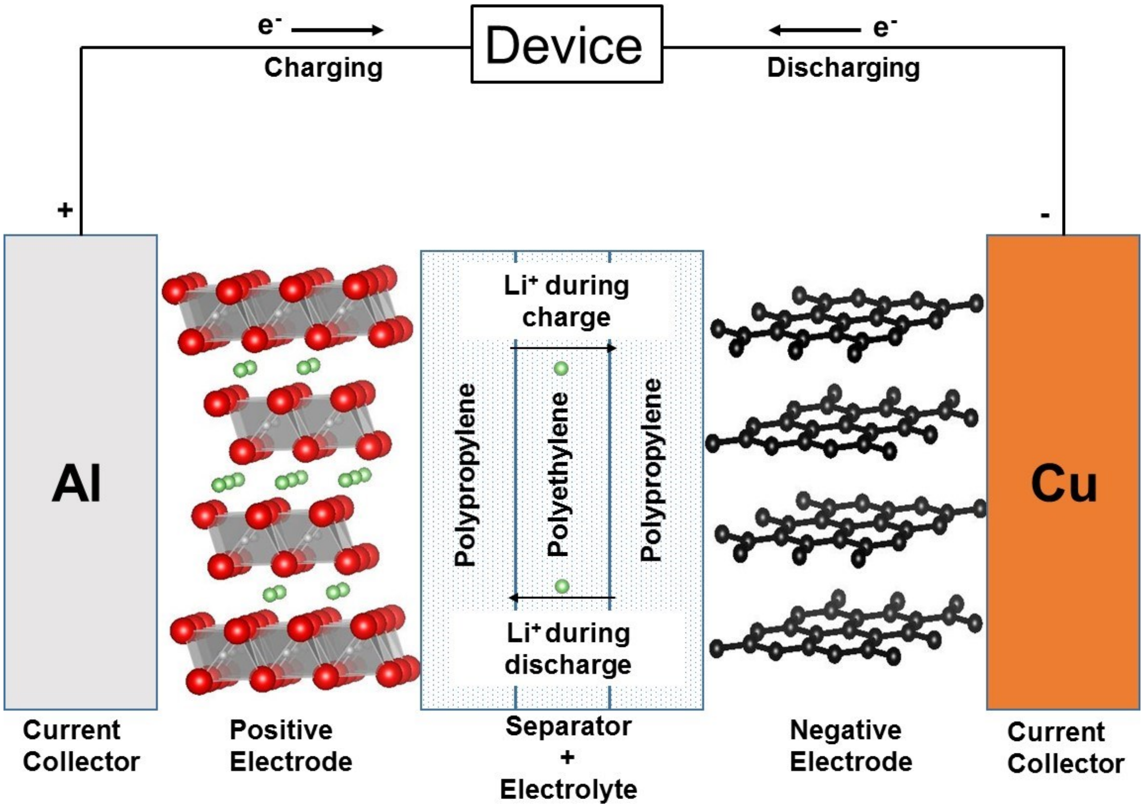

Figure 1.3 Schematic diagram of a lithium-ion battery. A $LiMO_2$ positive electrode and graphite negative electrode are shown. Red, grey, green, and black spheres represent oxygen, transitional metal, lithium, and carbon atoms respectively.

During charge, the transition metal oxide is oxidized. Maintaining charge neutrality within $LiMO_2$, lithium ions are removed from the metal oxide framework and then inserted in between graphite layers via the ion conducting electrolyte, which is also electrically insulating. Electrons removed during the oxidation of the positive electrode travel through an external circuit. These electrons reduce the graphite electrode, maintaining charge neutrality with the inserted lithium ions. During discharge, the reverse process occurs where graphite is oxidized and $LiMO_2$ is reduced with Li reinserting in to the metal oxide framework. The reversible intercalation/deintercalation allows for rechargeable operation.

A schematic diagram of a sodium-ion battery is shown in Figure 1.4. The basic components are analogous to a lithium-ion battery, consisting of a positive electrode, separator, and negative electrode, all components are soaked with electrolyte. The positive and negative electrode can consist of a layered transition metal oxide ($NaMO_2$) and a disordered graphitic carbon (called hard carbon), respectively, in full cells. These electrode materials are again coated onto current collectors in order to enhance electrical conductivity. One particular advantage of sodium-ion batteries is that sodium does not alloy with aluminum at low voltages, so aluminum can be used for the negative electrode current collector, reducing cost of the battery. As in the lithium-ion case, the separator can be made of both high purity polyethylene and polypropylene where the polyethylene layer is sandwiched in between two polypropylene layers. Similarly, ion conducting electrolytes typically comprise of a sodium salt dissolved in an aprotic organic carbonate solvent. A significant disadvantage of sodium-ion batteries is the aforementioned hard carbon negative electrode. Hard carbon can only compete with graphite capacity in gravimetric terms, not volumetric terms, prohibiting the commercialization of sodium-ion cells for energy storage applications, including EVs where volumetric capacity is of utmost importance.[6]

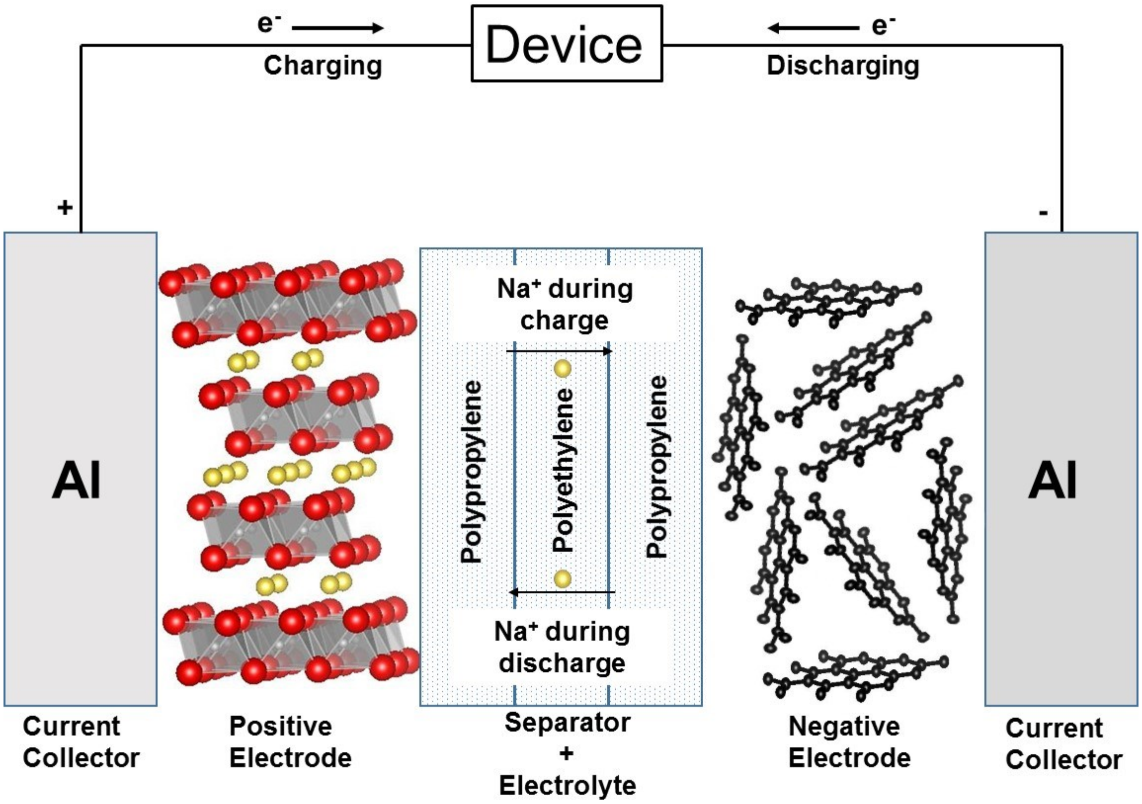

Figure 1.4 Schematic diagram of a sodium-ion battery. A $NaMO_2$ positive electrode and hard carbon negative electrode are shown. Red, grey, yellow, and black spheres represent oxygen, transitional metal, sodium, and carbon atoms, respectively.

1.2.2 Negative Electrode Materials for Sodium-Ion Batteries

The lack of practical high energy density negative electrode materials limits sodium-ion battery development. As described above, graphite is the most commonly used negative electrode material for lithium-ion batteries having a low voltage and high theoretical capacity of 372 mAh/g or 750 Ah/L. Note that the theoretical capacity, in mAh g^{-1} is given by:[18]

$$C = \frac{n_e F}{3.6 M_m} \tag{1.2}$$

where n_e is the number of electrons transferred in the reaction, F is Faraday’s constant of 96 485 C mol^{-1}, M_m is the molar mass of the active material in g mol^{-1}, and 3.6 is a factor in units of C mAh^{-1}. However, Na does not intercalate into graphite to a significant degree.[19] Reversible sodiation has been demonstrated in hard carbon, but its density is low, resulting in a low volumetric capacity (~450 Ah/L).[20] This limits the use of hard carbon as a practical negative electrode material motivating researchers to pursue other chemistries.

Group 14 and 15 elements that form binary compounds with Na show promise as negative electrode materials.[14] For example, reversible sodiation of Sn has been observed, with 864 mAh g^{-1} achieved upon full sodiation to $Na_{15}Sn_4$ (theoretical capacity 847 mAh g^{-1}).[21] Also, Sb/C composites have been demonstrated to deliver reversible capacities of 610 mAh g^{-1} with good rate capability (50% of capacity retained at 2000 mA g^{-1}).[22] Allotropes of phosphorus are also strong negative electrode candidates, with red phosphorus having high reversible capacities ≥1500 mAh g^{-1} between 0.0 – 0.8 V.[23] In general, large volume expansion involved with sodiation of these binary compounds, which can cause particle disconnection, and their high reactivity with electrolyte both limit commercial application.[14] Metal oxide materials might be able to overcome these issues while still having appreciable energy density.

1.2.3 Metal Oxides

Various metal oxide materials have shown promise as negative electrode candidates for Na-ion batteries as intercalation compounds. Specifically, titanium and vanadium oxides are of interest due to the low-voltage redox couples of $Ti^{3+/4+}$ and $V^{2+/3+}$. For example, the lowest voltage for any Na intercalation oxide compound studied to date is $Na_2Ti_3O_7$, with a reversible plateau around 0.3 V versus Na/Na^+ with a corresponding capacity of 200 mAh/g (~688 Ah/L).[24] Other low voltage titanates have recently been demonstrated as well, such as Na reversible intercalation in the vacancies in $Na_xNi_{x/2}Ti_{1-x/2}O_2$.[25,26] Polymorphs of TiO_2 have also shown promise, with reversible capacities of more than 150 mAh g^{-1} achieved within a voltage range of 0.0-2.0 V.[27] However, intercalation mechanisms have limited capacities due to the finite number of vacancies that Li and Na ions can occupy whereas the capacities in conversion reactions have the potential to be significantly larger.[26,28]

Conversion reactions in metal-ion cells are those in which an active electrode material, M_aX_b, reacts with an alkali metal ion, A, via an electrochemical displacement reaction, which may be represented by the general reaction:[29]

$$M_aX_b + (bc)A \rightleftharpoons aM + bA_cX. \tag{1}$$

Conversion reactions have been well studied in Li-ion batteries for both binary transition metal oxides and mixed transition metal oxides, where reactions go to completion to form Li_2O; an example using Fe_2O_3 is shown below:[30]

$$Fe_2O_3 + 6Li \rightleftharpoons 2Fe + 3Li_2O. \tag{2}$$

In this thesis, the theoretical capacity of these reactions were calculated based on conversion reactions going to completion, so that all of the oxygen has reaction with Li or Na to form Li_2O or Na_2O. Nanosized binary oxides such as Fe_2O_3, Co_3O_4, Mn_3O_4 and NiO have been found to have significant capacity via conversion reactions with Na (e. g. ~ 2000 Ah/L for Fe_2O_3).[31] The analogous reaction for Fe_2O_3 with sodium proceeds as follows:

$$Fe_2O_3 + 6Na \rightleftharpoons 2Fe + 3Na_2O. \tag{3}$$

While these materials have large reversible capacities it should be noted that the voltage range of 0 to 3 V they have been cycled within is not useful for a negative electrode material. One example of a mixed transition metal oxide negative electrode for Na-ion batteries is $NiCo_2O_4$ spinel, which has a reversible capacity of 884 mAh/g with Li (close to its theoretical capacity) and 200 mAh/g (~1196 Ah/L) with Na when cycled from 0 to 3 V.[32] Co and Ni metal appear to be formed in the products after full lithiation, suggesting a conversion mechanism is occurring. As these volumetric capacities are significantly larger than hard carbon in sodium-ion cells, the potential for high energy density negative electrode materials via conversion reactions deserves more attention.

In order for conversion electrodes to compete with intercalation electrodes, many issues need to be solved. One of the most significant issues, voltage hysteresis, is demonstrated in Figure 1.5, where voltage curves are shown for sodiation/desodiation of $Na_{0.6}Ni_{0.3}Ti_{0.7}O_2$ and Fe_2O_3 as representatives of intercalation and conversion mechanisms, respectively.[26,33] The inefficiency between sodiation/desodiation is significantly larger in the case for conversion. Specifically, the coulombic efficiency (CE) of a given cycle is defined as:

$$CE = \frac{Q_c}{Q_d} \tag{1.3}$$

where Q_d is the discharge capacity and Q_c is the charge capacity of the subsequent half-cycle. The CE is typically lower for conversion reactions compared to intercalation reactions. Many investigations have been devoted to reducing this hysteresis through improving kinetics of materials with conductive additives and reducing particle size.[34] However, it has been shown recently that a large portion of this hysteresis can be attributed to a different chemical pathways upon reduction and oxidation, claiming that conversion electrodes may only remain a laboratory curiousity.[35] On the contrary, the lowest hysteresis for lithiation/delithiation of a conversion material has been reported recently of ~150 mV which is comparable to hysteresis of intercalation mechanisms.[36] If low average voltage and low hysteresis electrodes can indeed be synthesized, the significantly larger capacity of conversion electrodes can be taken advantage of (Fig. 1.5), leading to higher energy densities in both lithium-ion and sodium-ion batteries.

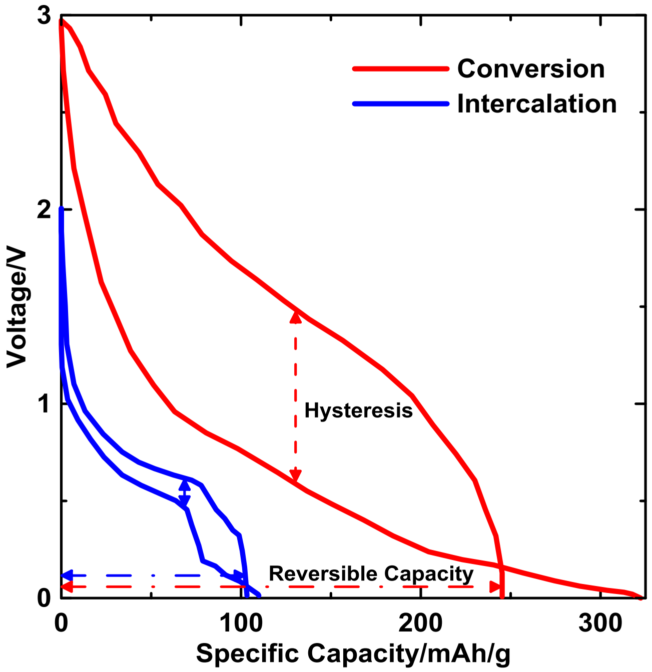

Figure 1.5 A comparison between intercalation and conversion negative electrode materials. Curves of $Na_{0.6}Ni_{0.3}Ti_{0.7}O_2$ and Fe_2O_3 redrawn from references 26 and 33, respectively.

1.3 ORGANIZATION OF THESIS

The goals of this thesis were to explore conversion materials for sodium-ion negative electrodes. Materials were characterized using electrochemical techniques, powder X-ray diffraction and Mössbauer Spectroscopy. Some materials were found to have large volumetric capacity, undergoing unique electrochemical mechanisms. The improvement of kinetics of binary oxides was also explored, with observation of significant capacity for a material normally electrochemically inactive with sodium at room temperature.

Chapter 2 describes the experimental characterization techniques, in detail, that were used during this thesis work. First, the theory behind powder X-ray diffraction is briefly explained, followed by the experimental setup used. Second, the theory behind Mössbauer spectroscopy is briefly explained, followed by the experimental setup used. Finally, electrochemical characterization techniques are described in detail.

Chapter 3 reports a study of mixed transition metal titanates and vanadates that were synthesized and electrochemically characterized in Na cells as well as Li cells for comparison. Some of these materials were found to have volumetric capacities that far exceeded that of Li in graphite. $Co_3V_3O_8$, $CoTiO_3$ and $Ca_5Co_4(VO_4)_6$ were found to have sodiation mechanisms that were not simple conversion reactions. $CoTiO_3$ in particular had low hysteresis and good reversibility, which is suggestive of an intercalation mechanism.

Chapter 4 investigates the thermoelectrochemical activation of metal oxides. The sodiation of Fe_2O_3 is used as a case study to determine the effect of temperature increase on the electrochemistry of metal oxides that undergo conversion mechanisms. Then, a metal oxide that is normally inactive with sodium at room temperature, CoO, is activated by reducing crystallite size and one high temperature discharge such that it has significant reversible capacity at room temperature.

Chapter 5 provides general conclusions to the thesis and a future outlook on metal oxide conversion negative electrodes for sodium-ion batteries.

CHAPTER 2 EXPERIMENTAL TECHNIQUES

2.1 POWDER X-RAY DIFFRACTION

Powder X-ray diffraction (XRD) was used to characterize the crystal structure of materials synthesized in this work. XRD is a common technique used for the identification of crystalline solids and for elucidation of new crystal structures. A brief explanation of basic concepts are described below; complete explanations can be found elsewhere.[37, 38]

2.1.1 Bragg Diffraction

X-ray diffraction in a crystalline solid can be described by the Bragg law:

$$n\lambda = 2dsin\theta \qquad (2.1)$$

where n is an integer indicating the order of reflection from a plane in the crystal lattice, λ is the wavelength of the incident X-rays, d is the spacing between the planes in the crystal lattice, and θ is the angle between the incident X-rays and the diffracting planes. An illustration of the Bragg law is shown in Figure 2.1. The incident X-rays are diffracted by atomic planes, which is possible due to the similarities in size of λ and d (0.1 to 100 Å). The X-rays can diffract such that destructive and constructive interference can occur, where the latter satisfies the Bragg law. The constructive interference depends on the spacing of atomic planes as well as the specific elements that make up the crystal lattice. This makes XRD a versatile technique because XRD patterns are specific to the material, allowing for meaningful characterization.

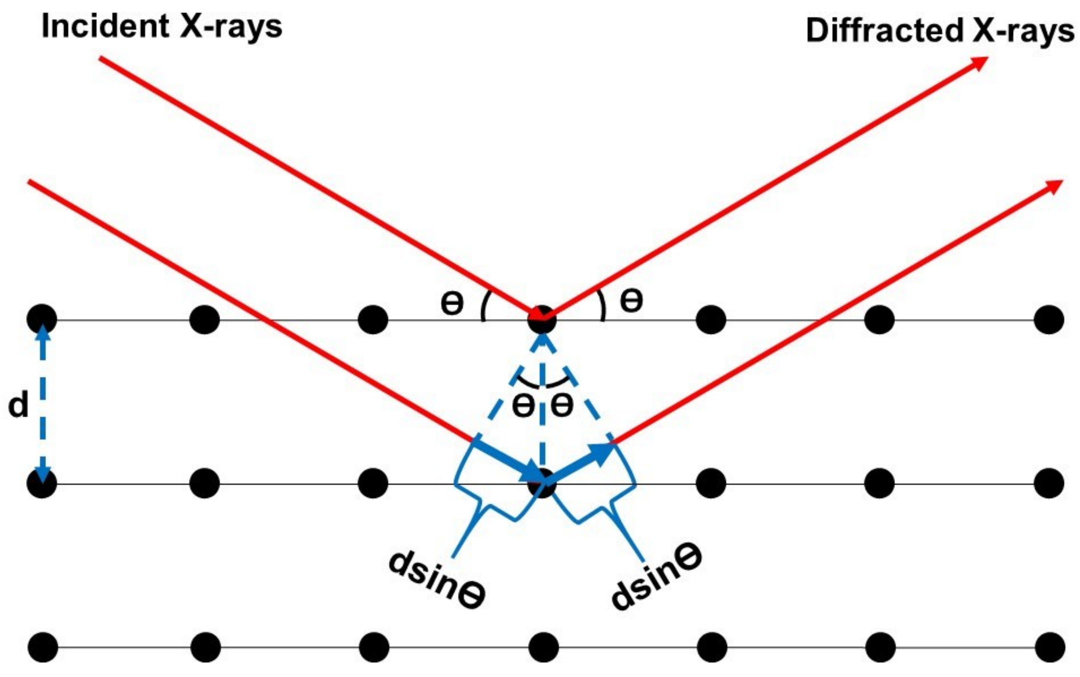

Figure 2.1 An illustration showing Bragg diffraction in a crystal lattice.

2.1.2 X-ray Diffraction Patterns

The total reflected intensities of an XRD pattern result from five factors according to[37]

$$I(\theta) = I_0 P(\theta) L(\theta) F^2(hkl) M(hkl) DW(hkl) \tag{2.2}$$

where I_0 is the intensity of incident radiation, $P(\theta)$ is the polarization factor, $L(\theta)$ is the Lorentz factor, $F(hkl)$ is the geometric structure factor, $M(hkl)$ is the multiplicity factor and $DW(hkl)$ is the Debye-Waller factor. The polarization factor corrects for changes in polarization of the incident beam by the sample and monochromator, which depends on the scattering angle. The Lorentz factor is a geometrical factor that arises because the powder crystallites are randomly oriented. Overall, the geometric structure factor accounts for the scattering from the contents in the unit cell in a crystal, given by

$$F(hkl) = \sum_1^N f_n(\theta) e^{2\pi i(hx_n + ky_n + lz_n)} \tag{2.3}$$

where $f_n(\Theta)$ is the atomic scattering factor for each atom in the unit cell, h, k, l are Miller indicies of the specifc Bragg plane and x_n, y_n, z_n are fractional atomic coordinates. The multiplicity factor takes into account diffracting planes that have the same d-spacing. Finally, the Debye-Waller factor accounts for thermal vibrations of atoms within the crystal.

For small crystallites, the crystallite size can be estimated from peaks in the XRD pattern by the Scherrer equation:[37]

$$t = \frac{K\lambda}{B\cos\Theta} \tag{2.4}$$

where t is the average dimension of the crystallite, λ is the wavelength of incident X-rays, K is a constant (typically 0.9 as a first approximation), B is the full width at half maximum of the diffraction peak in radians and Θ is the angle between incident X-rays and diffracting planes. Equation 2.4 is applicable for crystallite sizes on the order of 1 to 100 nm.[37]

XRD patterns of samples were measured using a Rigaku powder diffractometer X-ray system equipped with both a scintillation spot detector and a linear detector. The scintillation detector with a diffracted beam monochromator was used to measure XRD patterns of powder samples and ex situ XRD samples of electrodes. A D/TeX Ultra linear detector with K-beta filter was used for in situ XRD measurements. The Rigaku system was equipped with a Cu target X-ray tube and a Bragg-Brentano Θ:2Θ geometry. A filament current of 40 mA and an accelerating voltage of 45 kV were typically used to generate the X-rays. For XRD measurements, powder samples that were not stable in air were loaded into a gas tight X-ray sample holder (DPM Solutions, Hebbville NS), assembled in an argon filled glovebox. The sample holder had an aluminized Mylar window mounted in an arc such that it was perpendicular to the incident and scattered X-ray beam and did not contribute to the measured XRD patterns. X-ray diffraction data were collected for each sample at a typical scattering angle (2Θ) range of 10 to 80 degrees with a step of 0.05 degrees and a three second dwell time.

2.2 MÖSSBAUER SPECTROSCOPY

Mössbauer spectroscopy was used to study the sodiation of α-Fe_2O_3 different temperatures. Due to the amorphous nature of the sodiated products, X-ray diffraction experiments could not provide enough insight into their structure. The Mössbauer effect is the emission or absorption of a γ-ray photon without loss of energy due to recoil of the nucleus and without thermal broadening. A brief explanation of basic concepts are described below; complete explanations can be found elsewhere.[39, 40]

2.2.1 Recoil-Free Fraction

The energy of an isolated atom in the gas phase is defined as:

$$E = E_e - E_g \tag{2.5}$$

where E_e and E_g are the excited and ground states of the nucleus, respectively. One dimensional γ-ray emission for a gas phase atom is shown schematically in Figure 2.2.

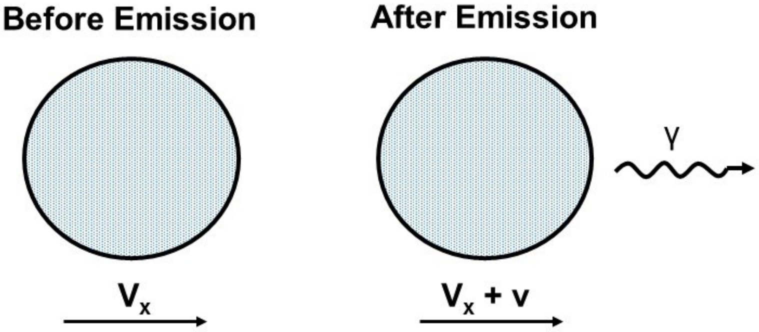

Figure 2.2 Emission of a γ-ray photon in one dimension. Adapted from reference 39.

If a nucleus of mass M is moving with an initial velocity V_x, then its total energy above the ground state at rest at the moment of emission is

$$E_{tot} = E + \frac{1}{2}MV_x^2. \tag{2.6}$$

After emission the total energy is

$$E_{tot} = E_\gamma + \frac{1}{2}M(V_x + v)^2 \tag{2.7}$$

where E_γ is the energy of the γ-ray photon and $V_x + v$ is the new velocity due to recoil (v can be positive or negative). The difference between the energy of the nuclear transition and energy of the emitted γ-ray photon is

$$\delta E = E - E_\gamma = \frac{1}{2}Mv^2 + MV_x v = E_R + E_D \tag{2.8}$$

where E_R and E_D are the recoil kinetic energy and a Doppler-effect energy, respectively.

The mean Doppler-effect energy $\overline{E_D}$ can be written in terms of the recoil kinetic energy:

$$\overline{E_D} = 2\sqrt{\overline{E_k}E_R} \tag{2.9}$$

where $\overline{E_k}$ is the mean kinetic energy per translational degree of freedom of a free atom in a gas with random thermal motion. Alternatively, E_R can be expressed as

$$E_R = \frac{E_\gamma^2}{2Mc^2} \tag{2.10}$$

where c = $2.998\text{x}10^8$ m s^{-1}, the speed of light. The mass M of the single emitting atom can be considered to the mass of the whole crystal if the emitting atom is unable to recoil freely because of chemical binding. This is possible because chemical binding and lattice energies in solids are on the order of 1-10 eV, significantly larger than typical free-atom E_R values (10^{-4} to 10^{-1} eV). Due to the relatively large mass of whole crystal, E_R approaches zero by equation (2.10) and, consequently, $\overline{E_D}$ approaches zero by equation

(2.9). Further, a fraction f of γ-ray photons are emitted without transfer of recoil energy to the vibrational states. The probability of this happening is called the recoil-free fraction and is described by the equation:

$$f = 1 - \frac{E_R}{\hbar\omega} \tag{2.11}$$

where $\hbar$ is the reduced Planck constant and ω is the photon angular frequency. When these above conditions are satisfied, δE approaches zero and hence overlap of the emission and absorption peaks increases, with $E = E_\gamma$, shown in Figure 2.3.

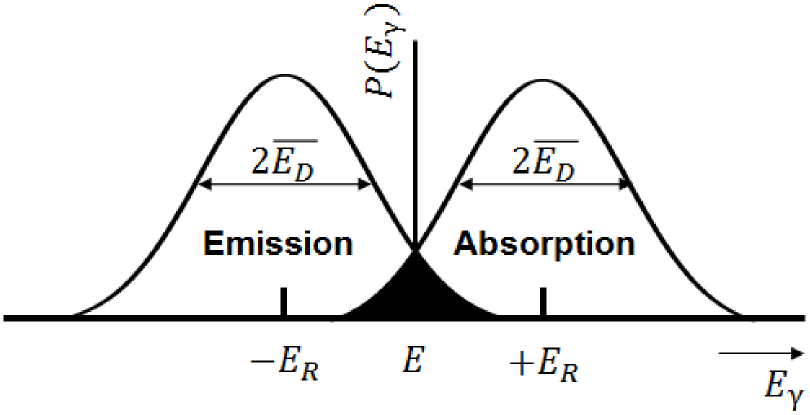

Figure 2.3 Resonance overlap for free-atom nuclear gamma resonance. Adapted from reference 39.

Radioactive nuclei that emit γ-ray photons allow for practical application of Mössbauer spectroscopy. Fortunately, the radioactive isotope ^{57}Co decays with a relatively long half-life of 270 days such that an abundant source of γ radiation from ^{57}Fe is available. This decay scheme is shown in Figure 2.4, where the transition from $\frac{3}{2}$ to $\frac{1}{2}$ is important for the Mössbauer effect. Further, the abundance of ^{57}Fe in natural iron is ~2%, making iron a practical element to study using Mössbauer spectroscopy.

In order to obtain a Mössbauer spectrum, the energy of incident γ-rays must be modulated to probe energy levels of Mössbauer nuclei. The modulation is achieved by

Doppler shifting the energies of γ-rays by $\frac{v_s}{c}E_\gamma$, where v_s is the velocity of the source. A velocity range of -10 mm/s to 10 mm/s was used to scan absorber energies in this work. Calibrations were performed with α-Fe which has a Mössbauer spectrum comprising of well-known features.[39]

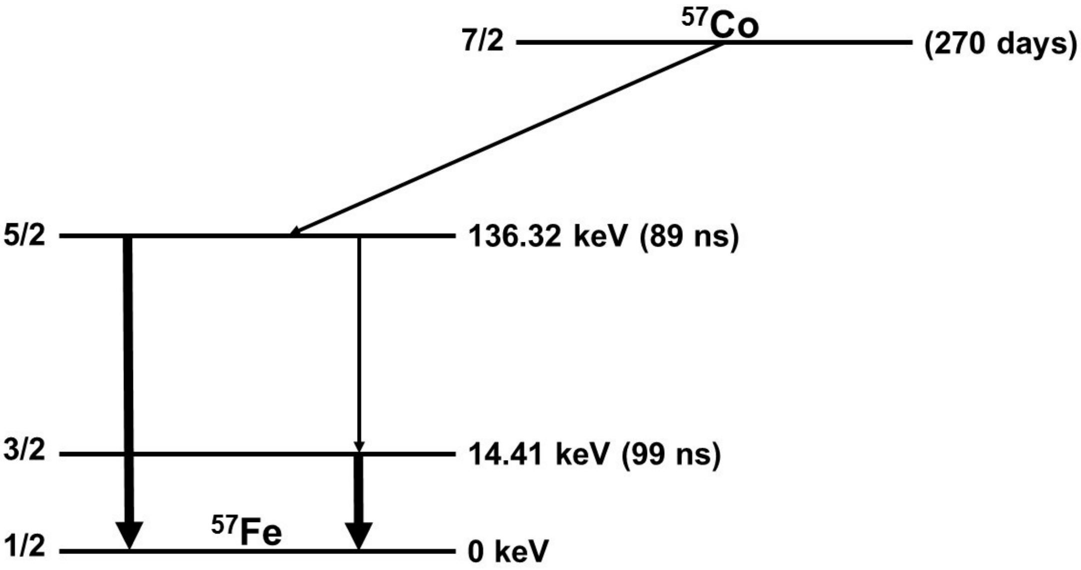

Figure 2.4 Decay scheme of ^{57}Co. Adapted from reference 39.

2.2.2 Hyperfine Interactions

Three types of hyperfine interactions were used to characterize local Fe environments of materials in this work. These three interactions were the isomer shift, quadrupole splitting, and Zeeman Effect. Through computer fitting of these interactions in Mössbauer spectra, the environments of Fe nuclei of materials in this work were characterized.

The s-electron density at the nucleus of an atom is affected by its surrounding chemical environment. In Mössbauer spectroscopy, the s-electron density of nuclei of interest is compared to reference nuclei (the γ-ray source, α-Fe, in this work) and this measurement is termed the chemical isomer shift. The chemical isomer shift, δ, is given by[39]

$$\delta = const * \{|\Psi_s(0)_A|^2 - |\Psi_s(0)_B|^2\} \tag{2.12}$$

where $const$ describes a nuclear term, $\Psi_s(0)_A$ and $\Psi_s(0)_B$ are the non-relativistic Schrödinger wavefunctions at r = 0 for the source and absorber, respectively. If the source and absorber are in identical chemical environments, the isomer shift will be zero. A difference in chemical environments of the source and absorber results in the resonant peak of the spectra being displaced from zero. For ^{57}Fe Mössbauer spectroscopy a positive isomer shift indicates a decrease in s-electron density in the absorber compared to the source. The isomer shift is defined for 0 K; the center shift that is discussed in chapter four is the isomer shift plus a relativistic temperature dependent contribution.

Nuclei in states with an angular momentum quantum number I greater than $\frac{1}{2}$ have a non-spherical charge distribution, which produces a nuclear quadrupole moment. This quadrupole moment can interact with the electric field gradient that results from a non-spherical charge distribution around a nucleus according to[39]

$$E_Q = \frac{e^2qQ}{4I(2I-1)}[(3I_Z^2 - I(I+1)] \tag{2.13}$$

where I_Z is the spin quantum state, Q is the nuclear quadrupole moment for the resonant isotope, and eq is the maxium value of the electric field gradient. The magnitude of the quadrupole interaction is given by the term e^2qQ. For crystallography isotropic samples, the prescence of quadrupole splitting results in two lines of equal intensity in the Mössbauer spectra (i. e. a symmetric doublet) for the $\frac{3}{2}$ to $\frac{1}{2}$ transition. The centroid of the doublet corresponds to the isomer shift.

The presence of a magnetic field at the nucleus results in the nuclear Zeeman Effect (or magnetic hyperfine splitting). The magnetic field interacts with nuclear energy levels according to[39]

$$E_m = -g\mu_N H m_I \tag{2.14}$$

where H is magnetic field flux density, g is the nuclear g-factor, μ_N is the nuclear Bohr magneton and m_I is the magnetic quantum number (z component of I). An illustration of all three hyperfine interactions is shown in Figure 2.5.

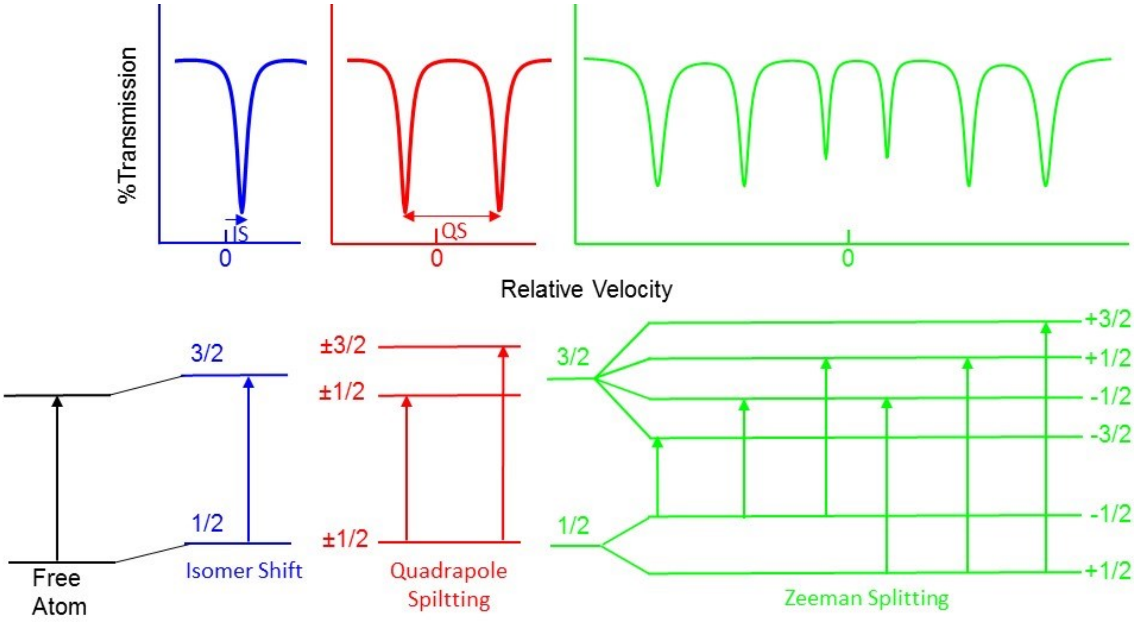

Figure 2.5 Illustration of hyperfine interactions with typical Mössbauer spectra. Adapted from reference 40.

Room temperature ^{57}Fe Mössbauer effect measurements were performed using a See Co. constant acceleration spectrometer equipped with a Rh^{57}Co source. Ex-situ Mössbauer measurements were performed on α-Fe_2O_3 electrodes that had been cycled in Na half-cells, as prepared in section 2.3.1. Sufficient material was collected by sodiation of four to six 16 mm diameter electrodes to 5 mV. The electrode material was recovered by scraping electrode material off the steel foil in an argon filled glovebox. The recovered powder was transferred to a sample holder which was heat sealed under argon.

The velocity scales for all spectra were calibrated relative to room temperature α-Fe. All Mössbauer spectra were analyzed with the Recoil software package (© 1998 Ken Largarec and Denis G. Rancourt). Pure Lorentzians were used in the fittings, where the peak width was allowed to vary in order to compensate for the distribution of iron environments.

2.3 ELECTROCHEMICAL TECHNIQUES

2.3.1 Electrode Fabrication

Electrodes consisted of active material, carbon black (Super P, Erachem Europe or Super C, Timcal) and polyvinylidene fluoride (PVDF, Kynar HSV 900) or polyimide (PI, HD MicroSystems PI 2555) binder in 80:10:10 or 80:12:8 weight ratios. These components were thoroughly mixed in N-methyl-2-pyrrolidone (Sigma Aldrich, anhydrous 99.5%) with two tungsten carbide balls in a Retsch PM200 rotary mill (100 rpm, 30 minutes) to create a uniform slurry. The slurry was then coated onto aluminum, copper or steel foil and dried under vacuum at 120 °C for 1 hour. Electrodes with PI binder were cured at 300°C under argon for one hour in order to undergo a condensation polymerization reaction. Electrodes with aluminum foil current collectors were used for Na cells only. Circular electrodes, 1 cm^2 in area, were punched from the resulting coatings for coin cells and 2 cm^2 for Conflat cells.

2.3.2 Half Cells

2325 type coin cells were assembled to evaluate the electrochemical performance of electrode materials in Li and Na half cells. Coin cell preparation was carried out in an argon filled glove box. Li and Na foil disk anodes were punched from foil 0.015″ (0.38 mm) thick that was rolled from thick Li foil (99.9%, Sigma Aldrich) or a Na ingot (Sigma Aldrich, ACS reagent grade), respectively. The electrolyte was 1 M $LiPF_6$ or $NaPF_6$ (Sigma Aldrich 98%) dissolved in 50:50 ethylene carbonate:diethyl carbonate by volume, with 10% by mass monofluoroethylene carbonate (all from BASF). Two Celgard 2300 and one BMF (blown microfiber separator, 3M Company) were used as separators. General assembly is shown in Figure 2.6.

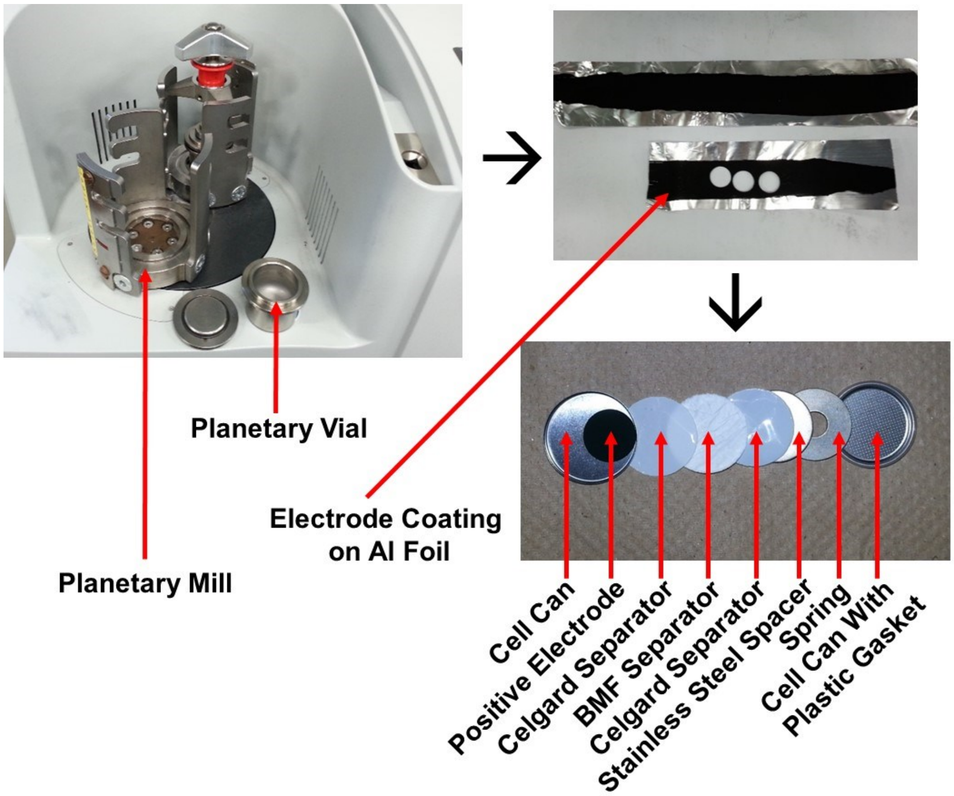

Figure 2.6 Schematic of the general process for preparing coin cells. Note that the stainless steel spacer is coated with lithium or sodium metal foil (not shown) for the negative electrode of the half cell.

Standard 2.125″ (53.18 mm) stainless steel Conflat vacuum fittings were purchased from Nor-Cal Products, Inc., Yreka, CA USA. Modifications to the fittings were made by DPM Solutions Inc. of Hebbville, NS Canada. These included drilling a 5/32″ (3.97 mm) hole into the rim of each fitting to a depth of 0.5″ (12.7 mm) to be used as female terminals for standard banana jack connectors. Double-sided Conflat fittings were provided with eight 1/4-28 threaded bolt holes (4 tapped holes are standard for 2.125″ fittings). Teflon and high density polyethylene sheet and tube stock were purchased from McMaster-Carr of Aurora, OH. Gaskets were punched from sheet stock using a press and circular cutting dies. Two Celgard 2300 and one blown microfiber separator (BMF, 3M Company) were used as separators for measurements ≤ 60°C. Glass filter paper (25 mm diameter, GF/F, Whatman), dried at 200°C for four hours was substituted for BMF for cells cycled at temperatures above 60°C. Components are shown in Figure 2.7.

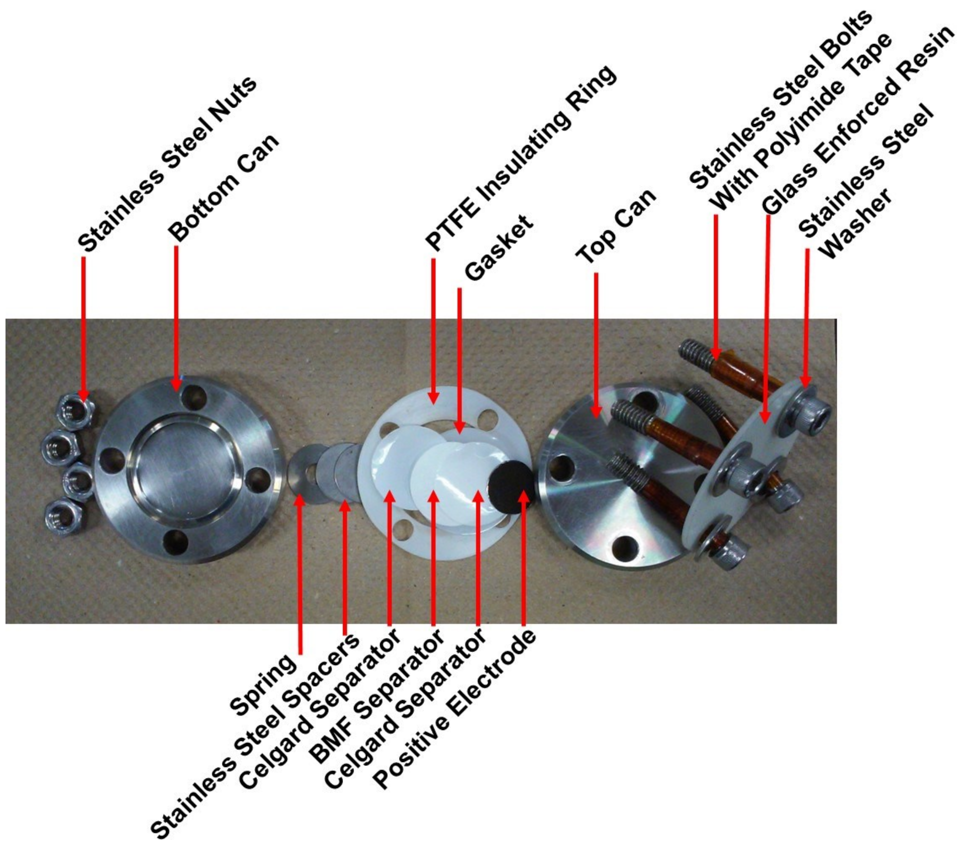

Figure 2.7 Components of a dry Conflat cell. Note that the stainless steel spacer was coated with lithium or sodium metal foil (not shown) for the negative electrode of the half cell.

2.3.3 Constant Current, Constant Voltage Measurements

Cells were tested with a Maccor Series 4000 Automated Test System (Maccor Inc., Tulsa, Oklahoma) with a current accuracy of 0.05% of full scale current. Most cells were cycled between 0.005 to 2.5 V, with some cycled between 0.005 to 4.3 V at constant currents of 15 mA/g with a trickle discharge (voltage held at 5 mV) to 7.5 mA/g. $TiVO_4$ and $MnTiO_3$ cells were cycled at constant currents of 3.75 mA/g with a trickle discharge to 1.875 mA/g. $CoTiO_3$ cells were cycled at constant currents of 17 mA/g with a trickle discharge to 8.5 mA/g.

Cells discussed in Chapter 4 were cycled at constant currents of 120 μA with a trickle discharge to 60 μA, at temperatures of 30°C, 60°C and 80°C. These currents correspond to approximately C/25 with a trickle to C/50 where C is the theoretical capacity and numerical values are the number of hours desired to complete a half cycle. Fe_2O_3 and CoO electrodes were also sodiated at 60°C, removed and transferred to new cells with fresh electrolyte and fresh sodium metal, and then cycled at 30°C. The high temperature cycling was performed in a 1.28 ft^3 Fisher oven that was coupled with a CN7500 Series ramp/soak temperature controller with a K thermocouple to measure temperature within ± 0.5°C.

CHAPTER 3 TITANATE AND VANADATE NEGATIVE ELECTRODE MATERIALS

3.1 INTRODUCTION

As described in section 1.2.3, metal oxides that undergo conversion reactions are of interest due to their high energy densities. In the past, mixed transition metal vanadates have been of particular interest for lithium-ion electrode materials because of vanadium's multiple oxidation states which provide opportunity for multiple reductions and thus large capacities can be achieved. These large capacities are in fact realized upon lithiation of several vanadates, however without full reduction of vanadium as described below, suggesting conversion is not the only mechanism contributing to this particular electrochemistry.[41–43]

The abnormally large lithiation capacity of $VFeO_4$ has been attributed to the role of O as a reaction centre since full reduction of V^{5+} to V metal was not observed.[43] A follow-up investigation had discovered evidence for full reduction of Fe^{3+} to Fe^0, along with simultaneous Fe^{3+} to Fe^{2+}, as well as partial oxidation of V^{5+} to V^{2+} at the end of discharge.[44] However, the observed capacity upon discharge corresponded to 8 Li atoms for this material, which would suggest full reduction of both Fe^{3+} and V^{5+}. It was proposed that lithium "adsorption" leads to Fe-"O-Li" and V-"O-Li" interactions and thus an abnormally large capacity.[44] A study of $VFeO_4 \cdot 1.1H_2O$ further demonstrated the dependence of reversible capacity on water content, supporting the "O-Li" adsorption mechanism.[45] Finally, it was rationalized that an acid-base reaction, where O^{2-} acts as a base to reversibly react with Li, contributes to the large reversible capacity for $VFeO_4$.[46]

Another example is the low voltage lithiation of brannerite-structured MnV_2O_6 which resulted in a large initial discharge capacity of 1400 mAh/g, accompanied by irreversible amorphization which is common for vanadates.[41] The large discharge capacity was subsequently followed by 800 mAh/g of reversible capacity upon cycling. Further investigations in to the redox mechanism has shown full reduction of Mn^{2+} to Mn^0 and partial reduction of V^{5+}.[47, 48] Upon charging, V^{2+} was observed to partially oxidize to V^{4+} while Mn^0 remained.[47] The irreversible capacity was attributed to this unchanged Mn^0 state and again the O anions are believed to be contributing to the abnormally large capacity.[47] The undesirable voltage curve hysteresis associated with conversion reactions can also be attributed to the role of O in the redox process, as breaking strong Li-O bonds during delithiation has a higher activation barrier compared to removing inserted Li from an open framework.[42]

The success in obtaining large capacities with lithium encourages the investigation of the sodiation of mixed vanadates. Fernandez de Luis *et al.* investigated MnV_2O_6 as a sodium-ion negative electrode material.[49] Incomplete conversion was observed, leading to a reversible capacity of 300 mAh/g with sodium. This incomplete conversion is attributed to the shift in potential of sodium compared to lithium (about 0.3 V), where part of the reduction of MnV_2O_6 would take place below the cut-off potential for the sodium case, leading to the relatively smaller observed capacity.

In this study, several mixed transition metal vanadates, along with titanates, were synthesized and their electrochemistry as negative electrodes were investigated in Na and Li half cells. Structural changes during sodiation were investigated by ex-situ and quasi in-situ X-ray diffraction. Low average voltage capacity was observed with unique voltage curves which are discussed.

3.2 SYNTHESIS AND CHARACTERIZATION OF TITANATES AND VANADATES

Several first row transition metal titanates and vanadates were synthesized via ball milling then heating stoichiometric amounts of as-purchased precursor reagents shown in Table 1. Ball milling was conducted with a Spex mixer-mill (SPEX CertiPrep) in 64 mL hardened steel ball-mill vials with two 0.5 in. hardened steel balls. The mass of the combined precursors never exceeded 6.00 grams. Non-stoichiometric amounts of precursors were only used in the synthesis of $Ca_5Co_4(VO_4)_6$, where a 1:1:1 atomic ratio of CaO, CoO and V_2O_5 were used. The ball milled powders were then heated in a tube furnace according to the conditions listed in Table 3.1. Compounds synthesized under argon were immediately transferred to an argon filled glove box without air exposure.

The XRD patterns of the prepared samples are shown in Figure 3.1 with the identifying Powder Diffraction File (PDF) number indicated.[50] Most materials were identified to be phase pure. Exceptions are $Ca_5Co_4(VO_4)_6$, which had a minor $Co_3V_2O_8$ impurity, and CoV_3O_8, $CrVO_4$, which had minor unidentified impurities.

Table 3.1 Milling/heating conditions for the preparation of materials.

End Product	**Precursors**	**Milling Conditions**	**Heating Conditions**
$CoTiO_3$ (ilmenite structure)	Co_3O_4 (<10µm, Sigma-Aldrich) TiO_2 (puriss, 99 – 100.5 %, Sigma-Aldrich)	Two hours in air	800°C for 10 hours in air
$MnTiO_3$ (ilmenite structure)	MnO_2 (60 - 230 mesh, > 99%, Sigma-Aldrich) TiO_2 (puriss, 99 – 100.5 %, Sigma-Aldrich)	One hour in air	1100°C for 10 hours in argon
$VFeO_4$ (triclinic $VFeO_4$ structure)	V_2O_5 (> 99.6%, Sigma-Aldrich) Fe_2O_3 (< 5 µm, > 99%, Sigma-Aldrich)	One hour in air	550°C for 24 hours in air
$Ca_5Co_4(VO_4)_6$ (cubic $Ca_5Co_4(VO_4)_6$ structure)	CaO (99.9%, Sigma-Aldrich) CoO (-325 mesh, Sigma-Aldrich) V_2O_5 (>99.6%, Sigma-Aldrich)	One hour in argon	750°C for 10 hours in argon
$Co_2V_2O_7$ (dichromate structure)	Co_3O_4 (<10 µm, Sigma-Aldrich) V_2O_5 (> 99.6%, Sigma-Aldrich)	One hour in air	600°C for 30 hours in air
CoV_3O_8 (orthorhombic α-CoV_3O_8 structure)	CoO (-325 mesh, Sigma-Aldrich) V_2O_4 (99.9% trace metals basis) V_2O_5 (> 99.6%, Sigma-Aldrich)	One hour in argon	600°C for 12 hours in argon
$Mn_2V_2O_7$ (thortveitite structure)	MnO (-60 mesh, 99%, Sigma-Aldrich) V_2O_5 (> 99.6%, Sigma-Aldrich)	One hour in air	600°C for 30 hours in air
MnV_2O_6 (brannerite structure)	Mn_2O_3 (-325 mesh, 99%, Sigma-Aldrich) V_2O_5 (> 99.6%, Sigma-Aldrich	One hour in air	800°C for 30 hours in air
$CrVO_4$ (orthorhombic β-$CrPO_4$ structure)	Cr_2O_3 (50 µm, > 98%, Sigma-Aldrich) V_2O_5 (> 99.6%, Sigma-Aldrich)	One hour in air	800°C for 30 hours in air
$TiVO_4$ (pseudo rutile structure)	TiO_2 (puriss, 99 – 100.5 %, Sigma-Aldrich) V_2O_5 (> 99.6%, Sigma-Aldrich)	30 minutes in argon	1000°C for 16 hours in argon

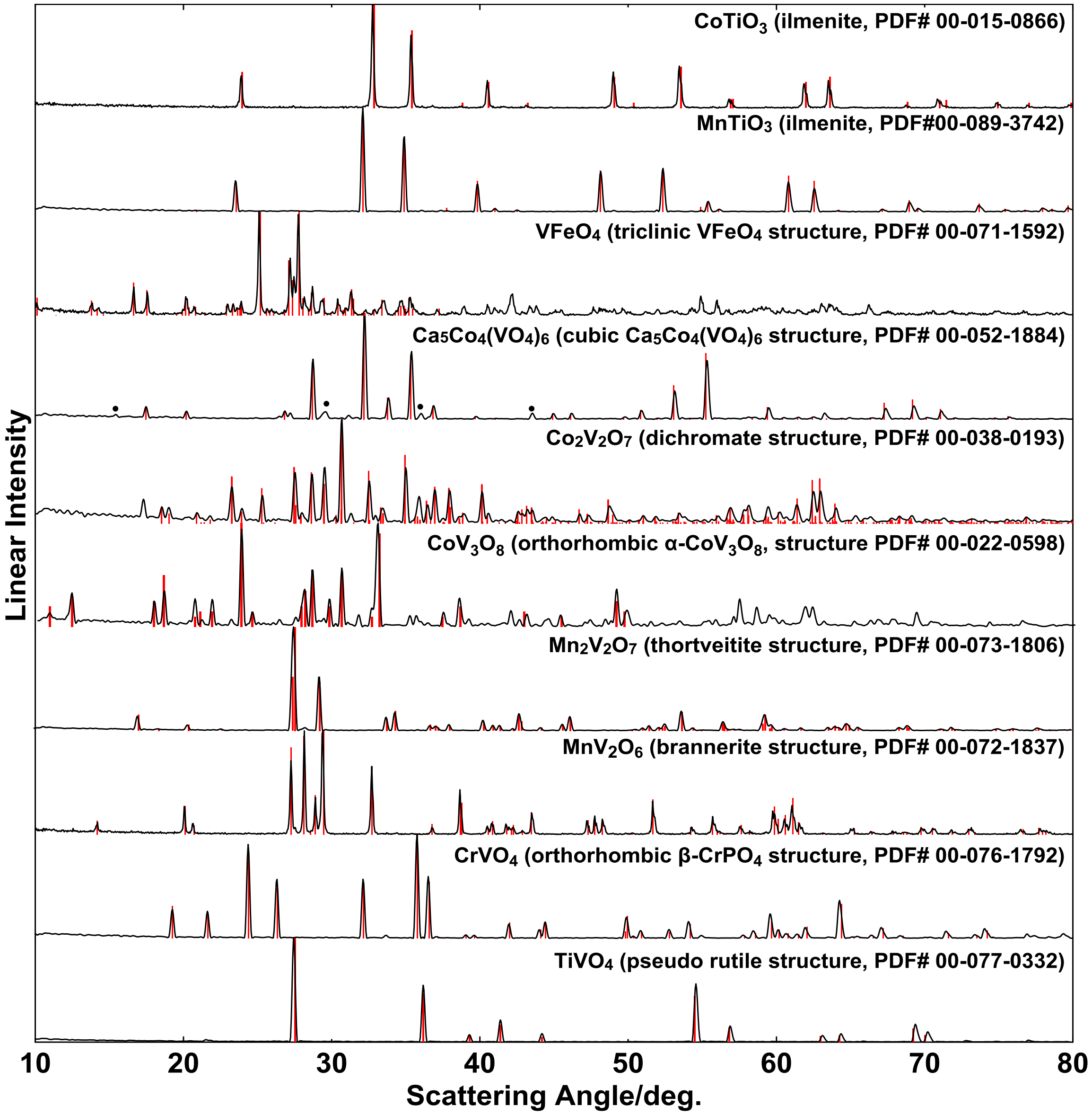

Figure 3.1 XRD patterns of all synthesized materials and their matching reference patterns. Black circles indicate the $Co_3V_2O_8$ impurity (PDF# 00-070-1393) phase found with $Ca_5Co_4(VO_4)_6$.

3.3 ELECTROCHEMICAL CHARACTERIZATION OF TITANATES AND VANADATES

All electrodes consisted of 80/10/10 active material/SP/PVDF by mass were spread on aluminum current collectors and cycled in coin cells as described in Chapter 2. Figure 3.2 shows the voltage curves of all the materials studied vs. lithium and vs. sodium. The lithiation capacities are comparable to those previously reported, with abnormally large capacities observed for $VFeO_4$ and MnV_2O_6.[42,49,51] To the knowledge of this author, the lithiations of $Mn_2V_2O_7$, $TiVO_4$, $Ca_5Co_4(VO_4)_6$ and CoV_3O_8 at low voltages have not been reported experimentally before. The voltage curves of $VFeO_4$, $Co_2V_2O_7$, $Mn_2V_2O_7$, CoV_3O_8, and MnV_2O_6 vs. lithium have high first discharge lithiation capacities, large reversible capacities and large voltage curve hysteresis. These features are typical of materials that undergo conversion reactions. $Ca_5Co_4(VO_4)_6$ and $CoTiO_3$ have lower first lithiation capacities and lower hysteresis. Such features are atypical of conversion reactions, and will be discussed in detail later. Reversible sodiation occurs for $CoTiO_3$, $VFeO_4$, $Ca_5Co_4(VO_4)_6$, CoV_3O_8, and MnV_2O_6. The reversible capacity achieved for the sodiation of MnV_2O_6 is comparable to that found in the literature.[49] In general the initial sodiation capacities are much less than the lithiation capacities for all materials and are just a fraction of the theoretical capacity. No abnormally large capacities were observed for sodiation of these materials compared to what has been observed for lithiation of these material in the past. Thermodynamically these oxides should react completely with sodium to form reduced metals and sodium oxide. The low capacity observed is indicative that the complete conversion reaction is kinetically hindered. However, the lower voltage hysteresis for sodium cells seems to indicate that the reaction occuring is less kinetically hindered than a typical conversion reaction. All other materials were essentially inactive towards sodiation at 30°C. $CrVO_4$ and $TiVO_4$ were inactive towards Li and Na. This result is consistent with Denis *et al.*[42], where orthorhombic $CrVO_4$ was also found to be electrochemically inactive with Li.

Figure 3.3 shows the observed reversible capacities versus the theoretical capacities for all of the materials studied. These values are tabulated in Tables 3.2 and 3.3. Excepting $VFeO_4$, all materials have observed capacities that are far below the theoretical capacity based on a full conversion reaction. This suggests that either the conversion reactions are incomplete or that lithiation/sodiation proceeds via a different mechanism. As mentioned above, most of the materials studied have significantly larger reversible lithiation capacities compared to their reversible sodiation capacities, with a fraction of the theoretical capacity achieved in sodium cells. $VFeO_4$ has the largest lithiation and sodiation capacities suggesting it is the most electrochemically active material studied. The compounds containing Co consistently have more sodiation capacity than Mn compounds, even when comparing isostructural $CoTiO_3$ and $MnTiO_3$. It is not clear why this should be the case. Although the reversible sodiation capacities are generally much smaller than that of Li, the volumetric sodiation capacities for some compounds are nevertheless quite large. In fact MnV_2O_6, CoV_3O_8, and $VFeO_4$ (820 - 1163 Ah/L) all have reversible volumetric sodiation capacities that far exceed that of hard carbon (~450 Ah/L) and even that of graphite in a lithium ion cell (~730 Ah/L). However, the corresponding irreversible capacities for these Na cells are also significantly large.

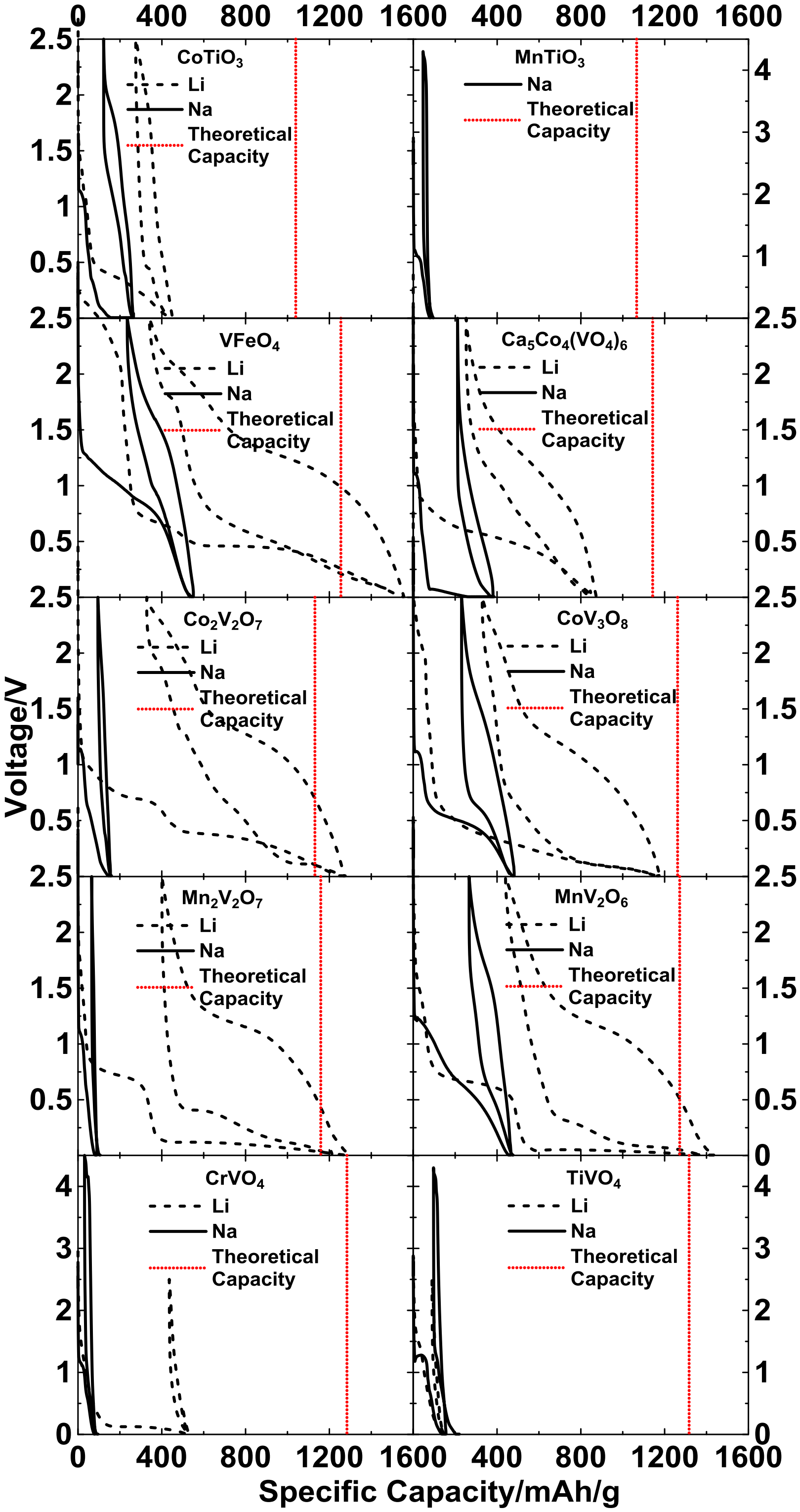

Figure 3.2 Observed reversible capacities of all materials studied vs. Li (dashed line) and Na (solid line) with the theoretical capacity plotted as a red vertical line.

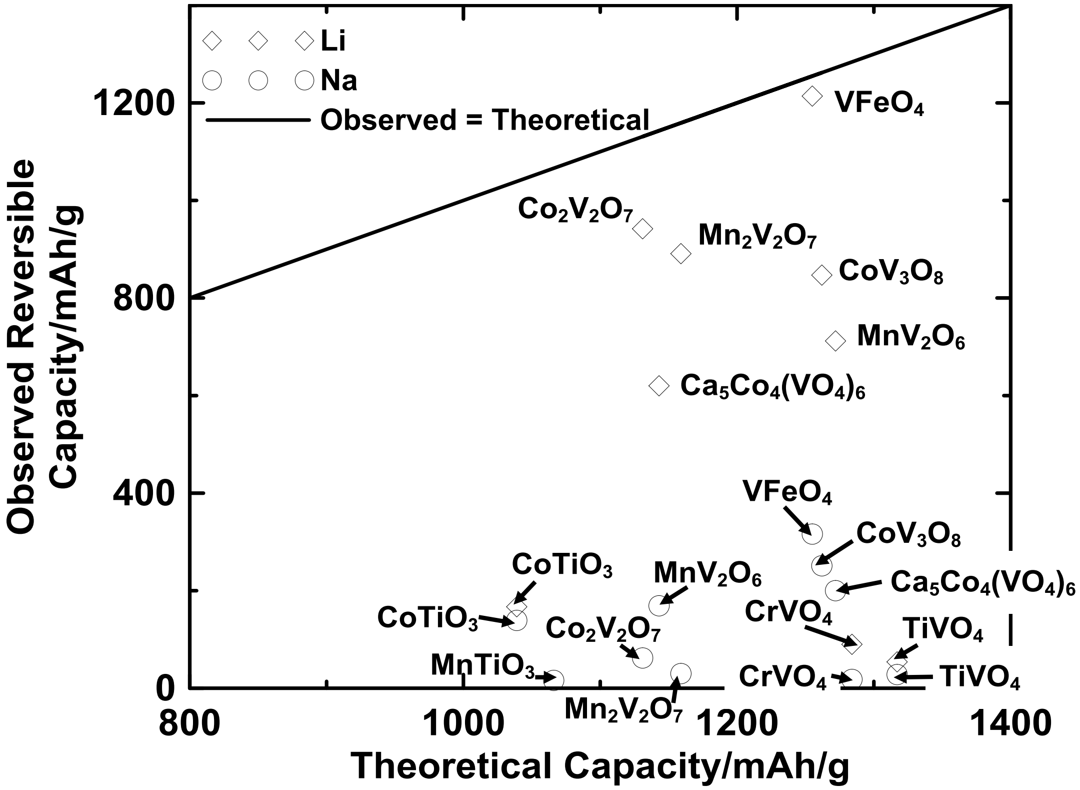

Figure 3.3 The observed reversible capacity vs. theoretical capacity for Li cells (diamond) and Na cells (circle) of all materials. A line indicating when the observed capacity is equal to the theoretical capacity is shown for comparison.

Table 3.2 Crystallographic densities, and reversible specific and volumetric capacities between 0 V and 2.5 V in Li cells of the metal oxides studied here.

Material	**Density / (g/cm^3)**	**Reversible Specific Capacity vs. Li / (mAh/g)**	**Reversible Volumetric Capacity vs. Li / (Ah/L)**
$CoTiO_3$	4.98	167	832
$MnTiO_3$	4.54	-	-
$VFeO_4$	3.68	1214	5696
$Ca_5Co_4(VO_4)_6$	3.70	620	2414
$Co_2V_2O_7$	4.28	942	4022
CoV_3O_8	3.8	847	3186
$Mn_2V_2O_7$	3.79	891	3393
MnV_2O_6	4.10	712	2855
$CrVO_4$	4.06	90	358
$TiVO_4$	4.37	54	236

Table 3.3 Crystallographic densities, and reversible specific and volumetric capacities between 0 V and 2.5 V in Na cells of the metal oxides studied here. Irreversible capacities for Na cells are also shown.

Material	**Density / (g/cm^3)**	**Reversible Specific Capacity vs. Na / (mAh/g)**	**Reversible Volumetric Capacity vs. Na / (Ah/L)**	**Irreversible Volumetric Capacity vs. Na/ (%)**
$CoTiO_3$	4.98	139	692	47
$MnTiO_3$	4.54	16	73	80
$VFeO_4$	3.68	316	1163	43
$Ca_5Co_4(VO_4)_6$	3.70	169	625	56
$Co_2V_2O_7$	4.28	62	265	60
CoV_3O_8	3.8	251	953	48
$Mn_2V_2O_7$	3.79	30	114	67
MnV_2O_6	4.10	200	820	57
$CrVO_4$	4.06	18	73	78
$TiVO_4$	4.37	28	122	82

Figure 3.4 shows the difference between the first charge mean voltage and second discharge mean voltage for the lithiation and sodiation for materials with significant reversible sodiation capacity, *i.e.* $CoTiO_3$, $VFeO_4$, $Ca_5Co_4(VO_4)_6$, CoV_3O_8, and MnV_2O_6. $Ca_5Co_4(VO_4)_6$ and $VFeO_4$ have the lowest voltage hysteresis in sodium cells, and $Ca_5Co_4(VO_4)_6$ also has the lowest hysteresis in lithium cells. In general the hysteresis values are similar to that of nanosized oxides with relatively low hysteresis, such as nano-Fe_2O_3 (0.75 – 1.0 V)[31], suggesting conversion mechanisms are possible in these reactions. However, this hysteresis reduces significantly during cycling in the case of $CoTiO_3$, as will be shown below.

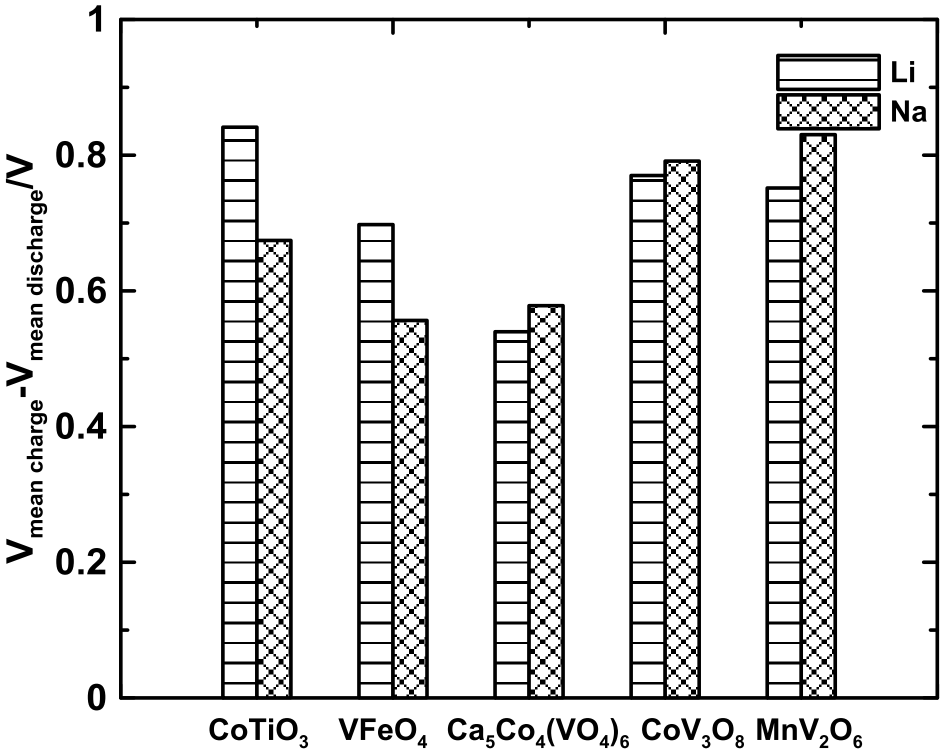

Figure 3.4 Difference between the first charge mean voltage and second discharge mean voltage for Li cells and Na cells of the materials studied with significant capacity below 2.5 V.

Figure 3.5(a) shows the 2nd cycle and 50th cycle of $CoTiO_3$ vs. Na. During the second charge, 128 mAh/g of reversible gravimetric capacity is observed, which shows capacity fade compared to the first charge of 139 mAh/g. The corresponding reversible volumetric capacity for the first charge is 692 Ah/L. This is significantly greater than the volumetric capacity of the sodiation of hard carbon and is also similar to the lithiation volumetric capacity of graphite in a lithium ion cell. The capacity faded significantly by cycle 30 and coulombic efficiency was poor as shown in Figure 3.5(b). However little capacity fade was observed after cycle 30, when the hysteresis had become low. During the 50th cycle the hysteresis decreased by almost a factor of two, to about 440 mV. This low hysteresis is atypical of a conversion reaction and is more suggestive of intercalation.

Apparently a material with good cycling characteristics and low hysteresis was formed during cycling. Nevertheless, cycling performance would still have to be improved for this material to have practical application.

Figure 3.6(a) shows the voltage curve for 2nd cycle of $Ca_5Co_4(VO_4)_6$ vs. Na. This material has a relatively low average desodiation voltage of about 0.90 V vs. Na and a reversible volumetric capacity is 625 Ah/L, again considerably exceeding the volumetric capacity of the sodiation of hard carbon. During the 50th cycle the hysteresis increases by a factor of two, to about 1.04 V. Also the capacity fades significantly, as shown in Figure 3.6(b). Clearly, compared to $CoTiO_3$, $Ca_5Co_4(VO_4)_6$ undergoes a different sodiation mechanism. Again, cycling performance would have to be improved for this material to have practical application.

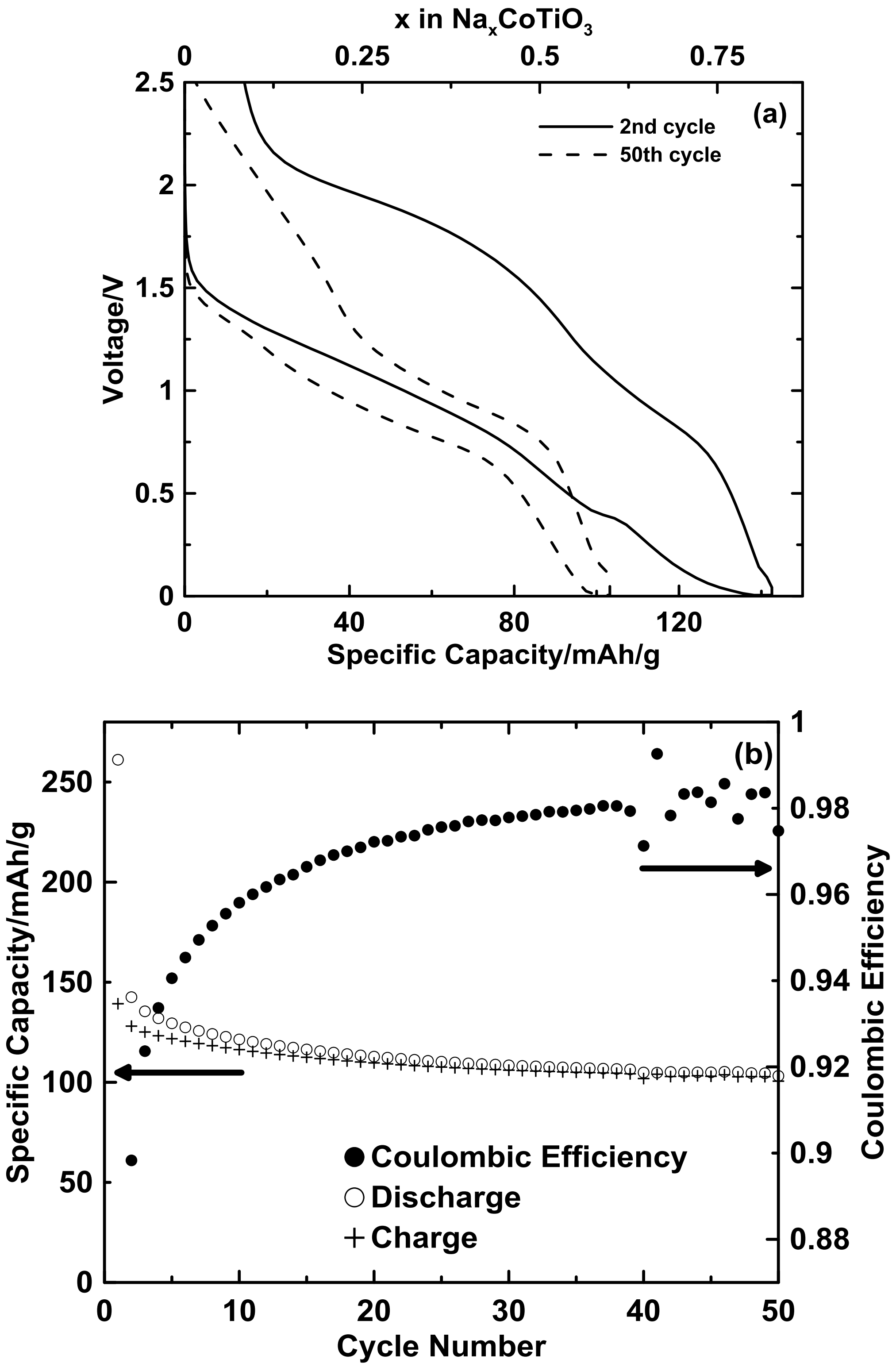

Figure 3.5 Voltage curves for the 2nd and 50th cycle (a) and the cycling performance (b) of $CoTiO_3$ vs. Na.

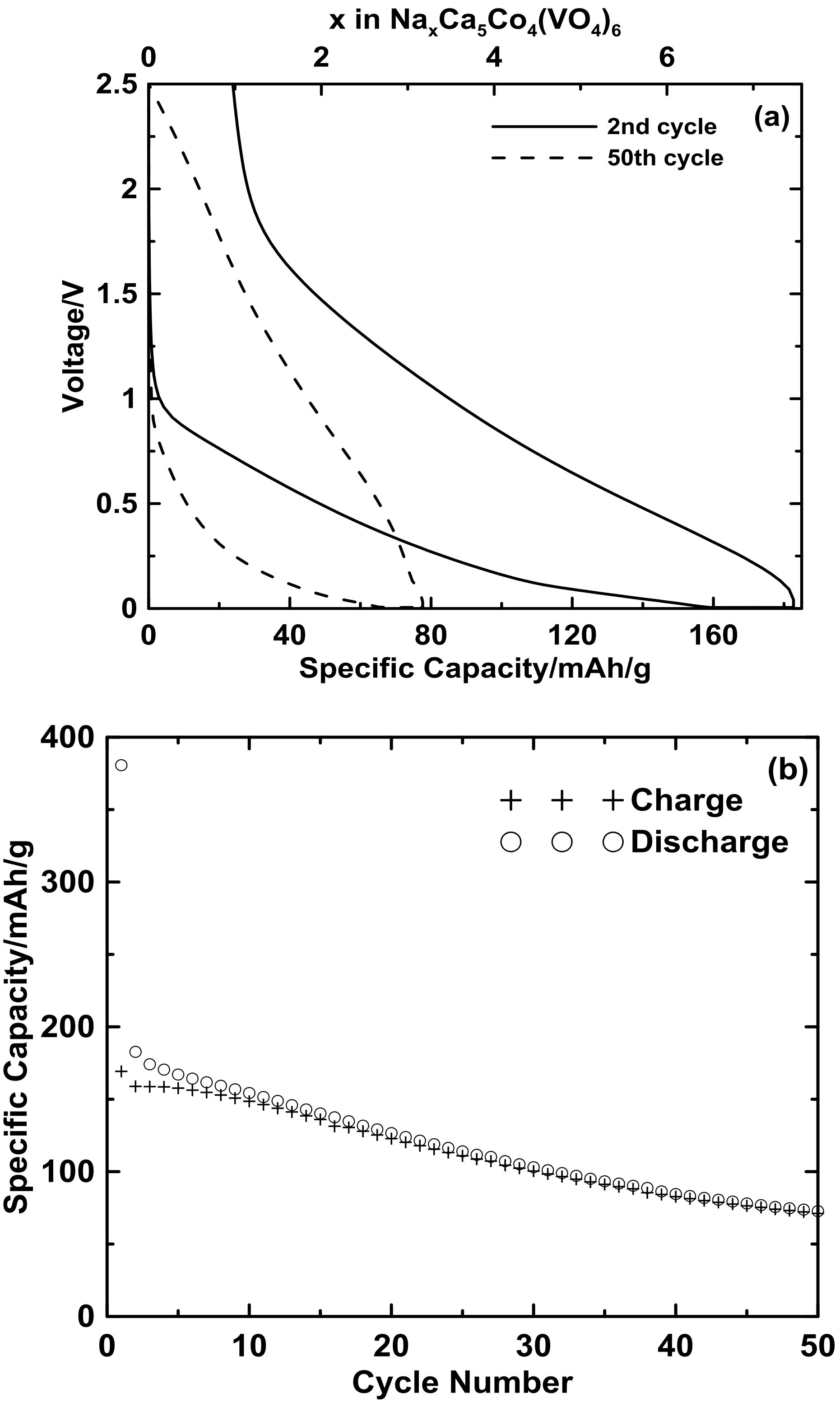

Figure 3.6 Voltage curves for the 2nd and 50th cycle (a) and the cycling performance (b) of $Ca_5Co_4(VO_4)_6$ vs. Na.

3.4 MECHANISTIC INVESTIGATION OF $CoTiO_3$, $Ca_5Co_4(VO_4)_6$ AND CoV_3O_8

Conflat cells (as described in section 2.3.2) constructed with the compounds $CoTiO_3$, $Ca_5Co_4(VO_4)_6$ and CoV_3O_8 were discharged under the same conditions as the coin cells described above. Electrodes were then carefully removed from the cells at different states of charge in an argon filled glove box. The coatings were scraped off the copper current collector and rinsed with dimethyl carbonate (Novolyte Technologies). The coating was then placed into a gas-tight sample stage under argon gas for XRD measurements. The stage has an arch shaped aluminized Mylar^{TM} window that does not contribute to the XRD patterns (DPM Solutions).

Ex-situ XRD patterns of fully sodiated $CoTiO_3$, $Ca_5Co_4(VO_4)_6$ and CoV_3O_8 are shown in Figure 3.7. The sharp peak below 20° as well as the broad peaks at about 44° are artifacts from the XRD sample holder (indicated by + in Figure 3.7). Other sharp peaks observed in the patterns correspond to unreacted precursors (indicated by ♦ in Figure 3.7), however these are small in area. All patterns demonstrate dramatic amorphization upon sodiation, which is remarkable, given that only a fraction of the theoretical capacity is accessed. For each of these oxides, this indicates that the entire material has taken part in the sodiation reaction, resulting in the destruction of the original structure. The low capacity of these materials compared to a full conversion reaction coupled with their reacting in their entirety during discharge, suggests a mechanism other than conversion is taking place. As mentioned in the introduction, complex reduction reactions involving oxygen are well known to occur during the lithiation of vanadates. Such mechanisms may also be occurring here. The development of a broad peak at approximately 41° was observed for sodiated $CoTiO_3$, which prompted further investigation in to its sodiation mechanism, and will be discussed below.

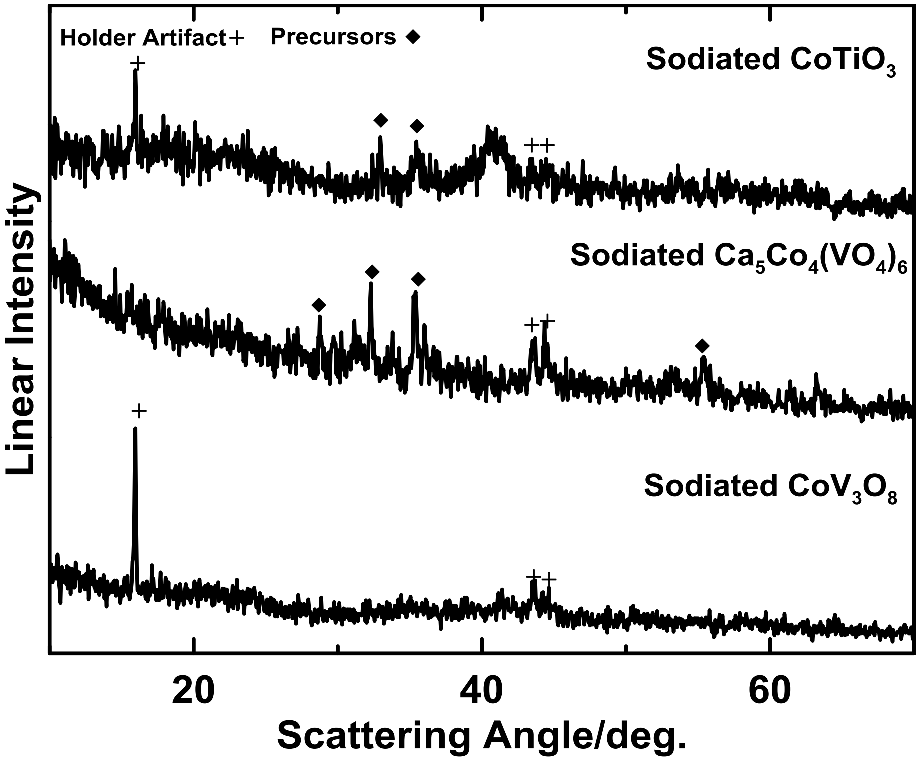

Figure 3.7 Ex-situ powder X-ray diffraction patterns for sodiated $CoTiO_3$, $Ca_5Co_4(VO_4)_6$, and CoV_3O_8. Artifacts from the air sensitive holder (+) and peaks of unreacted precursors (♦) are labelled.

The thickness of four fresh $CoTiO_3$ electrodes were measured to within ± 1µm with a Mitutoyo 293-340 precision micrometer. These electrodes were sodiated by discharging in a Na half cell under the conditions described above. Electrodes were then carefully removed from the cells in an argon-filled glove box and the electrode thicknesses were measured again. The coating volume was then determined by subtracting the thickness of the Al current collector and multiplying by the coating area. The measured volumes of the initial and sodiated $CoTiO_3$ electrodes were used to determine the volume expansion. The average initial coating thickness was 42 ± 2 µm. This corresponds to an average electrode porosity of 50%, which is a typical value for an uncalendered coating.[52] The average final coating thickness was 44 ± 2 μm. If the percent coating porosity is assumed to be constant during sodiation (as it is during the expansion of alloy coatings in lithium cells)[52], this corresponds to a surprisingly low volume expansion of only 6%. This low volume expansion is further evidence of an intercalation-type mechanism, and may explain the relatively good cycling observed for $CoTiO_3$.

Finally, $CoTiO_3$ was coated directly onto a beryllium disk with the same slurry compositions as described above. The Be disk served as both a current collector and as an X-ray window in a coin cell, so that XRD patterns could be obtained of the working electrode. Roscobond (Rosco Laboratories Inc.), a water-based contact adhesive, was used to affix the beryllium window to the inside of a coin cell can with circular hole cut in it. The coin cell was then assembled in the same manner as described above. After it was crimped shut, Torr Seal (Varian) was applied to the outside of the coin cell at the beryllium/coin cell can junction to ensure that the coin cell was properly sealed. A quasi *in-situ* procedure was used where the cell was cycled as described above, then paused at appropriate voltages while XRD measurements were performed. The cycling procedure was continued after each XRD measurement.

Figure 3.8 shows XRD patterns that were measured at open circuit at different points along the voltage curve of a $CoTiO_3$ vs. Na cell fitted with a Be window. The cell voltage curve is also shown, so that the XRD patterns can be correlated to the points in the voltage curve at which they were measured. Peaks consistently present for all XRD patterns are attributed to BeO and cell parts. During the first discharge, $CoTiO_3$ is consumed and a broad peak at approximately 41° appears as $CoTiO_3$ is sodiated. Subsequently, this broad peak disappears as the material is desodiated during the first charge. Furthermore, crystalline $CoTiO_3$ does not appear to be regenerated after charging. During the second discharge the broad peak at approximately 41° reappears as the material is sodiated. This broad peak likely does not correspond to CoO or Co, having main peaks at about 42° and 44°, respectively. It is possible that the broad peak at approximately 41° can be attributed to the main peak of $NaTiO_2$ with the R-3m (166) space group (PDF# 00-089-802). If this were the case, then, the following reaction can be proposed:

$$CoTiO_3 + Na \rightleftharpoons NaTiO_2 + CoO. \tag{4}$$

The theoretical capacity of this reaction is 173 mAh/g which is comparable to the observed reversible capacity of 139 mAh/g. This reaction would suggest a three phase mechanism is occurring. Recently, a three phase separation mechanism has been confirmed for the sodiation of $Li_4Ti_5O_{12}$.[53] Similar to the above mechanism, new phases that were formed were not distinguishable until near the end of discharge for the sodiation of $Li_4Ti_5O_{12}$, likely due to the sluggish nucleation and growth of new phases from slow Na^+ kinetics.[53] This supports the possibility of the suggested $CoTiO_3$/Na mechanism, however, a CoO phase was not observed and therefore more evidence is required. An alternate mechanism involves intercalation of disordered structures, similar to what has been investigated by Lee *et al*.[54] Given the amount of irreversible sodiation per cycle, enough Na may have been inserted into $CoTiO_3$ to form a percolating network amenable to intercalation. This supports the observation of decreased hysteresis for $CoTiO_{3.}$ Given these materials decompose to the amorphous state, Mössbauer spectroscopy (of Fe containing oxides), X-ray photoelectron spectroscopy, extended X-ray absorption fine structure spectroscopy and/or nuclear magnetic resonance studies may provide further understanding.

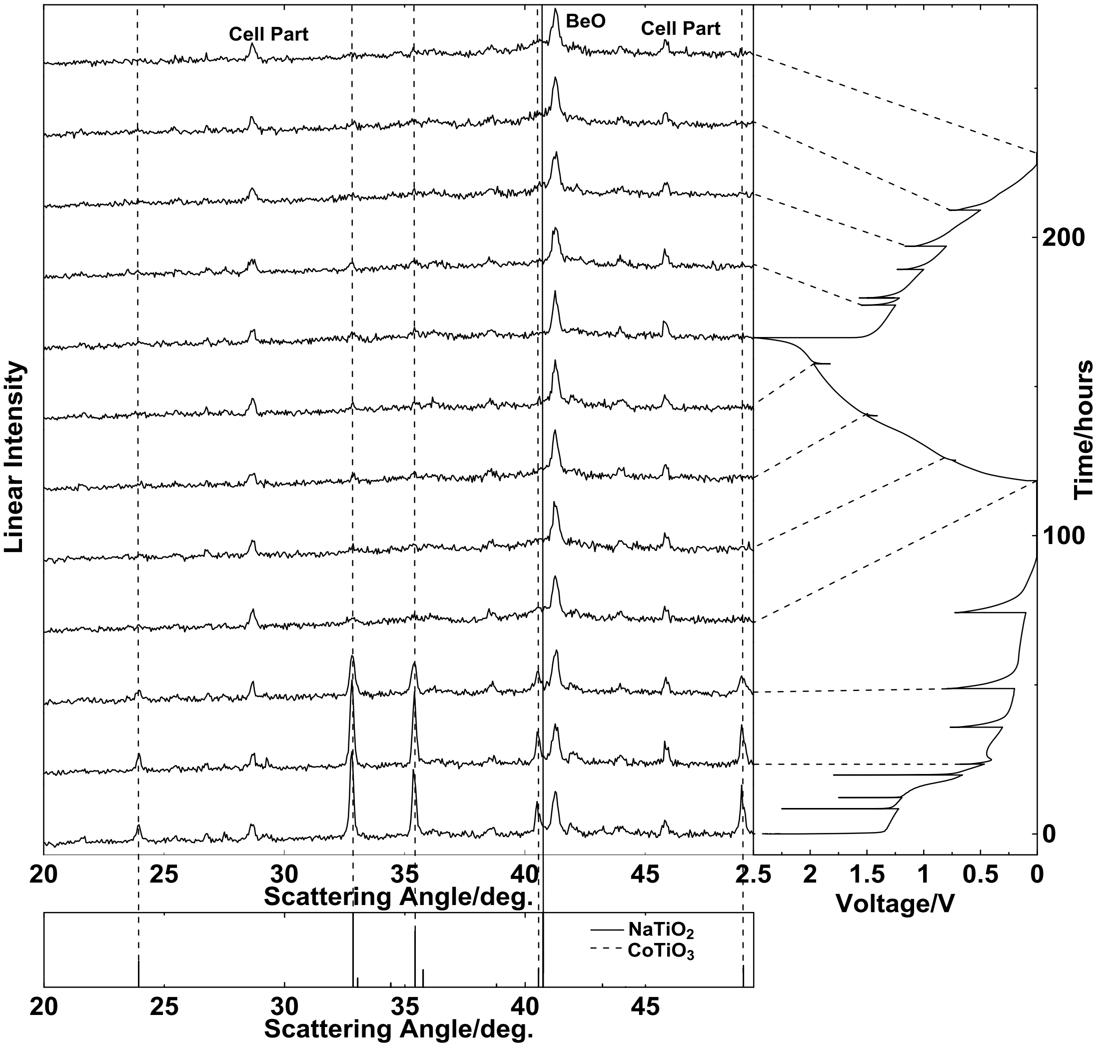

Figure 3.8 Quasi in-situ investigation of CoTiO$_3$/Na cell. The voltage vs. time curve on the right hand side indicates the voltages at which an X-ray pattern was collected. The main peaks for CoTiO$_3$ (dashed line) and NaTiO$_2$ (solid line) are shown below the experimental patterns.

3.5 CONCLUSION

Several mixed transition metal titanates and vanadates were synthesized and electrochemically investigated as anode materials in sodium and lithium cells. Most of these materials had significantly higher lithiation capacity than sodiation capacity, however all capacities were much lower than those for a full conversion reaction. Of these materials, $CoTiO_3$, $VFeO_4$, $Ca_5Co_4(VO_4)_6$, CoV_3O_8, and MnV_2O_6 exhibited significant volumetric capacities with sodium between 0.005 – 2.5 V. The volumetric capacities of these materials are much greater than the sodiation of hard carbon and, in some cases, greater than that for the lithiation of graphite. Fully discharged $CoTiO_3$, $Ca_5Co_4(VO_4)_6$, and CoV_3O_8 in sodium cells were found to be amorphous even though their capacity is only a small fraction of what would be predicted for a full conversion type reaction. Undesirable hysteresis was also observed.

$CoTiO_3$ was found to have particularly interesting characteristics as an anode in sodium cells. After 30 cycles the voltage curve hysteresis of $CoTiO_3$ reduced to only 440 mV. The volume expansion during sodiation was measured to be only 6%. Both the low hysteresis and low volume expansion are suggestive of an intercalation type mechanism. If such oxides could be made with low irreversible capacity they would be attractive for use as high volumetric capacity anodes in sodium-ion cells.

CHAPTER 4 ELECTROCHEMISTRY OF BINARY METAL OXIDES AT ELEVATED TEMPERATURES

4.1 INTRODUCTION

Binary transition metal oxides have been reported to have large reversible capacity with lithium via a conversion reaction, as explained in section 1.2.3, compared to materials that undergo intercalation mechanisms.[55] Other binary compounds that undergo conversion mechanisms have also been reported such as hydrides[56], sulfides[46], phosphides[57], nitrides[58] and fluorides[59]. There is considerable interest in taking advantage of these conversion reactions for both positive and negative electrode materials.[6,60] However, the large voltage hysteresis and poor cycling performance of these materials limit their commercialization. A sizeable research effort has been devoted to attempting to remove these limitations in the lithium-ion battery field.[6,60]

The origin of voltage hysteresis is not completely understood, with arguments for many kinetic origins being suggested.[6,35,60,61] The length of the lithium ion diffusion path into the binary oxide and electrolyte wettability of the electrode material are examples of kinetic factors that contribute to voltage hysteresis. Without optimizing the kinetics for an active material, large polarization of the cell can occur and thus shift the voltage curve to smaller (larger) values during discharge (charge), creating large hysteresis, and leading to low round trip energy efficiency.

Improvement of the kinetics has been achieved through, for example, particle size minimization, use of conductive coatings and porosity optimization.[6] Reducing particle size to the nanoscale has proven to be successful for accessing the majority of theoretical capacity of these binary materials, however this increase in interfacial area leads to more electrolyte decomposition.[60] In the case for binary oxides, this electrolyte decomposition creates extra capacity upon discharge that is enhanced by the metal nanoparticles formed during discharge (i.e. reduction of the metal oxide).[62,63] This is typically characterized by a sloping region below 0.8 V vs. lithium metal.[62,63] The exact nature of this reversible solid electrolyte interphase (SEI) is unknown, although it has been evidenced that ethylene oxide oligomers and lithium methyl carbonate can be formed for materials undergoing conversion reactions.[64] This SEI is also consumed upon charging (i.e. oxidation of the metal nanoparticle) and can reach reversible capacities as high as 150 mAh/g.[62] This gel-like polymer film can initially increase reversible capacity but eventually, due to its electrolyte consuming nature, leads to capacity fade.[62,65]

Recent studies have discovered that most of voltage hysteresis is associated with different reaction pathways occurring on charge and discharge rather than simple charge transfer polarization.[35,66] Success in reducing the hysteresis to a practical value (~150 mV) has been achieved by substituting Cu into the Fe lattice of the FeF_2 framework, forming the solid solution $Cu_yFe_{1-y}F_2$.[36] Such improvement of fundamental material composition may be the pathway to realizing small hysteresis conversion materials.

High temperature electrochemistry might be able to improve kinetic limitations. There are recent examples of activating materials through high temperature lithiation/delithiation of alloys and transition metal oxides such that they can reversibly cycle at room temperature.[67,68,69] This phenomena has been termed thermoelectrochemical activation.[69] With alloys, the high temperature cycling can create new phases that are electrochemically active with lithium.[67] For oxides, high temperature lithiation has been observed to reduce particle size of the conversion reaction products such that the activation energy is low enough for the reaction to proceed reversibly at room temperature.[68] To the knowledge of this author, these thermoelectrochemical procedures have not been reported for sodium-ion electrode materials.

Recently, binary compounds have become of interest for sodium-ion battery technology.[14] Given the standard molar Gibbs formation energy of Na_2O is larger than Li_2O, conversion reactions with binary oxides have a lower theoretical voltage with sodium metal.[29] This lower cell voltage is desirable for negative electrode materials. Binary transitional metal oxides such as Fe_2O_3, Fe_3O_4, Co_3O_4, Mn_3O_4, CuO, and NiO have been shown to have significant capacity with sodium.[14,29,31] Interestingly, oxides such as FeO and CoO have been found to have negligible electrochemical activity with sodium whereas significant capacity is observed with lithium.[70] Overall, as in the case for lithium, undesirable voltage hysteresis and cycling performance issues exist for these binary oxides with sodium. In this work, thermoelectrochemical routes were explored in attempt to both enhance and characterize the electrochemistry of α-Fe_2O_3 with sodium. Then, from what was observed with α-Fe_2O_3, two methods to electrochemically activate CoO are shown as well as what can be achieved by coupling these two activation methods.

4.2 EXPERIMENTAL TECHNIQUES

All electrodes were fabricated using active materials Fe_2O_3 (< 5 μm, > 99%, Sigma-Aldrich), CoO (-325 mesh, Sigma-Aldrich) or TiN (99.7% Alfa Aesar), combined with Super C carbon black (SC, Timcal) and polyimide (PI, HD MicroSystems PI 2555) binder as described in Chapter 2. These electrodes were characterized electrochemically using Conflat cells, and structurally using XRD and Mössbauer spectroscopy, as described in Chapter 2. Note that for (CoO/SC)/PI electrodes, (CoO/SC) represents a 8:1 mass ratio composite of CoO and SC that was synthesized by ball milling CoO (-325 mesh, Sigma-Aldrich) and SC for 2 hours using a Spex mixer-mill (SPEX CertiPrep) in 64 mL hardened steel ball-mill vials with five 0.5″ hardened steel balls. The mass of the combined (CoO/SC) never exceeded 3.00 grams. Also, (CoO/SC)/PI electrodes were prepared in an 80/10/10 by mass ratio compared to 80/12/8 for α-Fe_2O_3/SC/PI, TiN/SC/PI and CoO/SC/PI electrodes. All electrode coatings containing CoO were initially prepared in an argon filled glovebox and then dried in air.

4.3 ELECTROCHEMICAL AND STRUCTURAL CHARACTERIZATION OF FE_2O_3

The voltage curves of α-Fe_2O_3/SC/PI and TiN/SC/PI versus sodium metal at temperatures of 30°C, 60°C, and 80°C are shown in Figure 4.1. In the past, TiN has been used as a chemically inert component of electrode materials.[71] In this study, TiN/SC/PI coatings were used to characterize the capacity contribution from SC and PI components for electrodes comprising of a 80/12/8 mass ratio. The voltage curve for α-Fe_2O_3 at 30°C, in Figure 4.1(a), is similar to what has been observed for the sodiation/desodiation (discharge/charge) of α-Fe_2O_3 in previous literature.[31,33] Some irreversible sodiation is occurring, typically associated with electrolyte decomposition, as evidenced by the charge and discharge endpoint slippage of the voltage curve towards higher capacity values. Generally, during the first sodiation both α-Fe_2O_3 and TiN in Fig. 4.1(a)-(f) have increased capacity with temperature. However, upon subsequent desodiation/sodiations, α-Fe_2O_3 electrodes at 60°C (Fig. 4.1(c)) have significant increase in capacity with increase in temperature whereas the capacity from TiN electrodes (Figures 4.1(b), 4.1(d) and 4.1(f)) does not change significantly with increase in temperature. This suggests that

SC and PI contribute significantly to irreversible capacity and a small amount to reversible capacity for the α-Fe_2O_3 electrodes. At 80°C (Fig. 4.1(e)), the α-Fe_2O_3 cells are not able to cycle whereas TiN/SC/PI electrodes can, suggesting α-Fe_2O_3 is the main contributor to capacity fade for α-Fe_2O_3/SC/PI electrodes. At the higher temperature, excessive electrolyte decomposition can lead to SEI growth and electrolyte depletion such that the cell can no longer cycle.[62] Large volume changes associated with the desodiation/sodiation can also lead to electrically disconnected regions of the electrodes causing rapid cell failure.[72] Also, the average voltage hystereses between the first desodiation and second sodiation of α-Fe_2O_3 electrodes at 30°C and 60°C were 0.75 V and 0.67 V, respectively, indicating no significant change in hysteresis upon change in temperature. This observation agrees with similar studies of binary oxides at elevated temperatures.[35]

In order to calculate the capacities shown in Figure 4.2, the capacity contribution from SC/PI was calculated using the TiN electrodes and subtracted from the α-Fe_2O_3 electrodes. At 30°C, capacity increases during initial cycling, which has been attributed to the growth of the gel-like polymer film described in the introduction, as well as activation of the active material.[65] At 60°C, while larger initial capacities are realized, the capacity fades quickly. This could be due to accelerated electrolyte decomposition and/or large volume expansion/contraction of active materials upon sodiation/desodiation, as mentioned above. No cycling is observed at 80°C which was obvious in Figure 4.1(e).

It is worth noting α-Fe_2O_3 electrodes were initially coated onto copper foil and tested. The cycling performances at 30°C and 60°C are shown in Figure 4.3. Similar performance compared to steel foil is observed at 30°C, as expected, where the capacity initially increased before fade. However at 60°C the fade was much more dramatic than that of the steel electrodes, and in most cases these cells cannot cycle. This suggests parasitic reactions occur with the copper electrode at elevated temperatures. Therefore steel electrodes were chosen to carry out experiments.

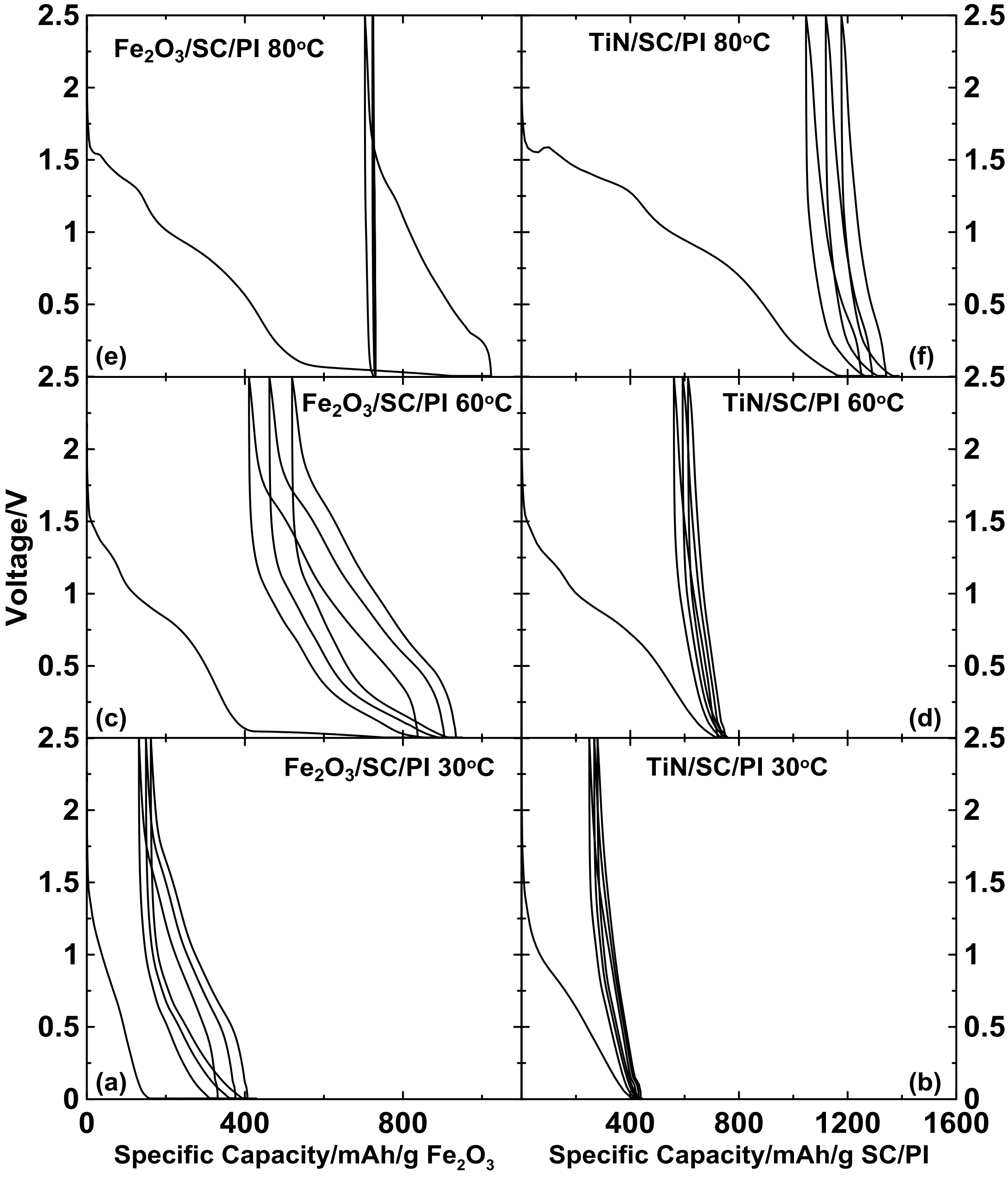

Figure 4.1 Voltage curves of α-Fe_2O_3/SC/PI and TiN/SC/PI Na half-cells cycled at C/30 with a trickle to C/60 at 30°C, 60°C, and 80°C.

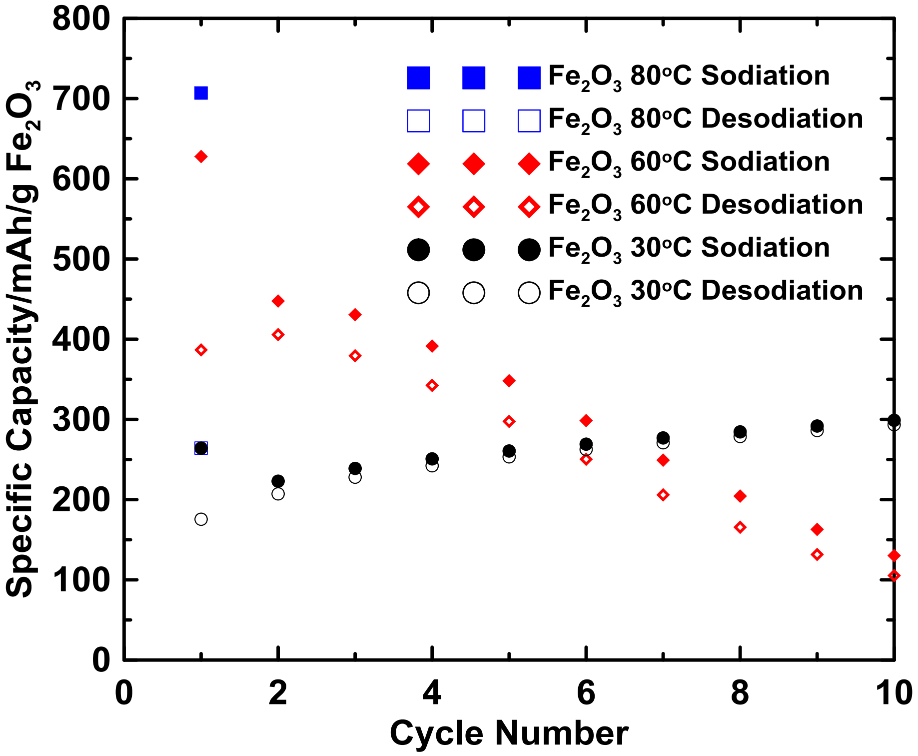

Figure 4.2 Cycling performance of α-Fe_2O_3 electrodes without SC/PI contribution at 30°C, 60°C, and 80°C.

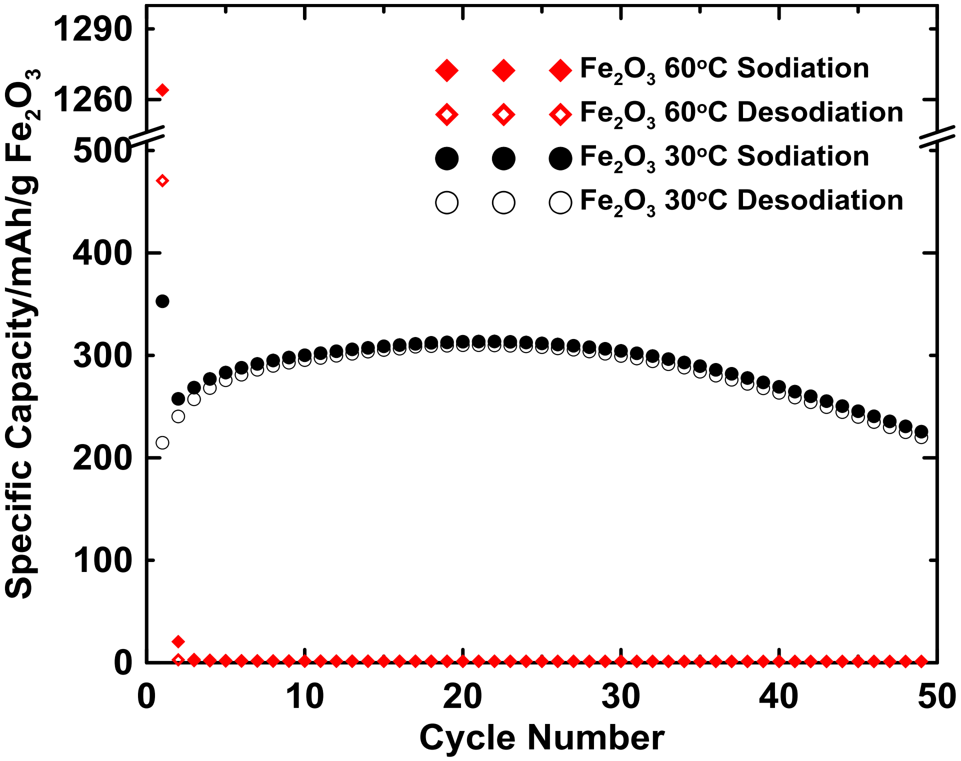

Figure 4.3 Cycling performance of α-Fe_2O_3/SC/PI on copper foil at 30°C and 60°C.

Mössbauer spectroscopy was used to investigate the sodiation mechanism of α-Fe_2O_3 at different temperatures. The center shift, quadrupole splitting, Zeeman splitting and peak widths are given in Table 4.1 for assigned phases in this investigation. Values from an investigation of the lithiation of α-Fe_2O_3 at room temperature are shown in parentheses for comparison.[73] The covariance matrix of the fit was used to evaluate parameter uncertainties. Generally the values compare well with the literature, with variation in some cases. This variation is likely due to the fundamental differences in the sodiation of Fe_2O_3 at different temperatures.

The Mössbauer spectra of the initial α-Fe_2O_3 electrode material along with the first and 27th sodiation (where the increasing capacity reached its maximum) of α-Fe_2O_3 are shown in Figure 4.4. After the first sodiation, a doublet attributed to superparamagnetic α-Fe_2O_3 (indicating small grains of α-Fe_2O_3) was observed. Apparently a crystallite size decrease in α-Fe_2O_3 happens upon initial sodation, which has been observed in the case for the lithiation of α-Fe_2O_3, and referred to as electrochemical grinding.[73] After 27 desodiation/sodiation cycles, the superparamagnetic α-Fe_2O_3 was present along with doublets associated with Fe^{2+} and surface Fe^0, and a singlet attributed to bulk Fe^0. Surface Fe^0 refers to iron that resides in a nonisotropic environment near grain boundaries, giving rise to a quadrupole-split doublet. This is possible with small crystallite size, where much of the iron is in the region of grain boundaries. This suggests a similar mechanism happens for the sodiation of α-Fe_2O_3 compared to the lithiation of α-Fe_2O_3, where crystallite size is decreased, followed by insertion of sodium into α-Fe_2O_3 (forming $Na_xFe_2O_3$) and finally a full reduction to Fe^0. The observations of these phases agree with other investigations of the sodiation of Fe_2O_3 over different voltage ranges and in composite materials.[33,74] It can be speculated that the increasing capacity during cycling is due to continuous growth of the gel-like polymer film as well as continuous activation of superparamagnetic α-Fe_2O_3.

Table 4.1 Mössbauer parameters used to fit all spectra. The center shift, quadrupole splitting, Zeeman splitting, and peak width are represented by δ, Δ, H_m, and Γ, respectively. Values from reference 73 are shown in brackets for comparison.

	δ (mm/s)	**Δ (mm/s)**	**H_m (kOe)**	**Γ (mm/s)**
α-Fe_2O_3	0.373±0.004 /0.378±0.003 (0.376/0.463)	-0.103±0.004 /-0.105±0.003 (-0.217/-0.197)	514.6±0.3 /516.5±0.3 (505/535)	0.11±0.01 /0.20±0.04 (0.295/0.50)
Super-paramagnetic α-Fe_2O_3	0.42±0.02 (0.36/0.44)	0.69±0.04 (0.60/0.76)		0.48±0.03 (0.67/1.15)
Fe^0 bulk	-0.21±0.03 /-0.07±0.02 (-0.15/0.03)			0.17±0.04 /0.56±0.02 (0.40/0.93)
Fe^0 Surface	0.27±0.05 /0.28±0.02 (0.11/0.21)	0.23±0.03 /0.55±0.07 (0.33/0.35)		0.18±0.05 /0.28±0.08 (0.030/0.86)
Fe^{2+} 30°C	1.13±0.03 (0.91/1.07)	1.03±0.06 (1.61/1.00)		0.36±0.03 (0.67/1.02)
Unidentified $Fe^{(x)}$ 80°C	0.77±0.02	0.50±0.02		0.25±0.02

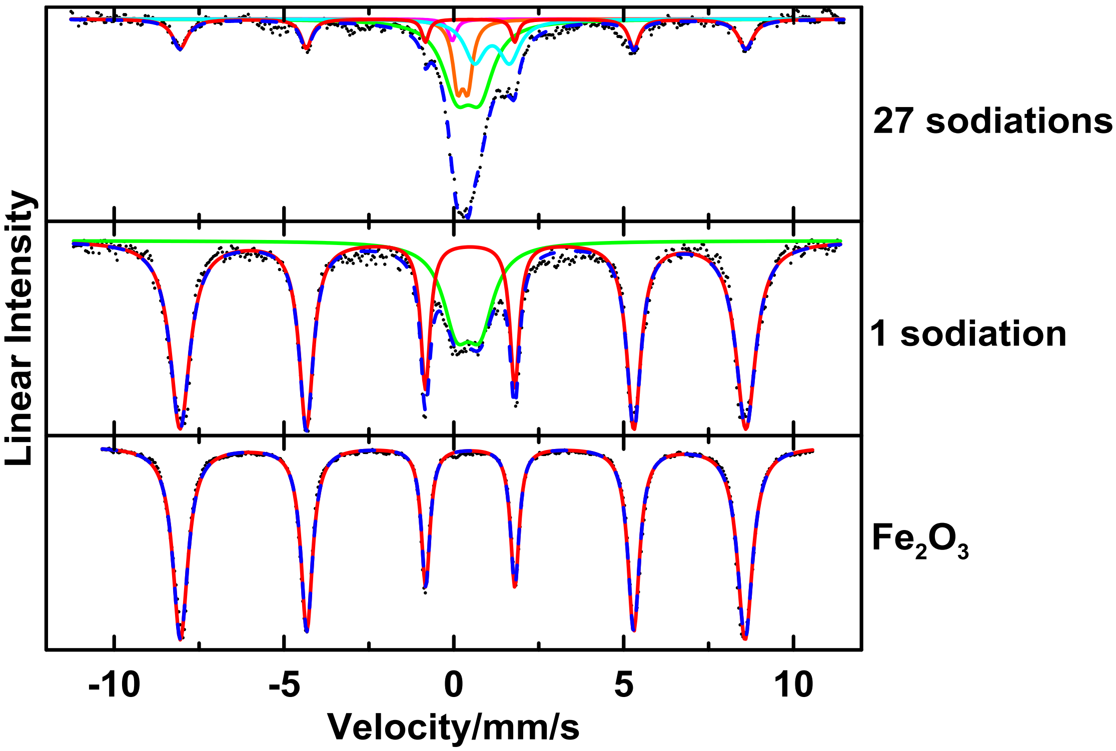

Figure 4.4 Mössbauer spectra of the initial α-Fe$_2$O$_3$ electrode material, the first, and 27th sodiations of α-Fe$_2$O$_3$.

The Mössbauer spectra of α-Fe$_2$O$_3$ after initial sodiations at 30°C, 60°C, and 80°C are shown in Figure 4.5. At 60°C, there is no evidence of Fe^{2+}, only superparamagnetic α-Fe$_2$O$_3$, surface Fe^0, and bulk Fe^0 phases. Clearly more α-Fe$_2$O$_3$ is consumed at 60°C compared to 30°C, suggesting the extra capacity observed at 60°C is not just electrolyte consumption and is indeed forming more products from the conversion reaction as well. At 80°C, even more α-Fe$_2$O$_3$ is consumed compared to 60°C but an unidentified Fe$^{(x)}$ species is observed along with the increase of the Fe^0 bulk phase. Given that the 80°C α-Fe$_2$O$_3$ cell was unable to cycle, the unidentified Fe$^{(x)}$ species may be associated with irreversible electrolyte decomposition around active particles. Further structural characterization is required for complete understanding for the reaction of α-Fe$_2$O$_3$ with sodium.

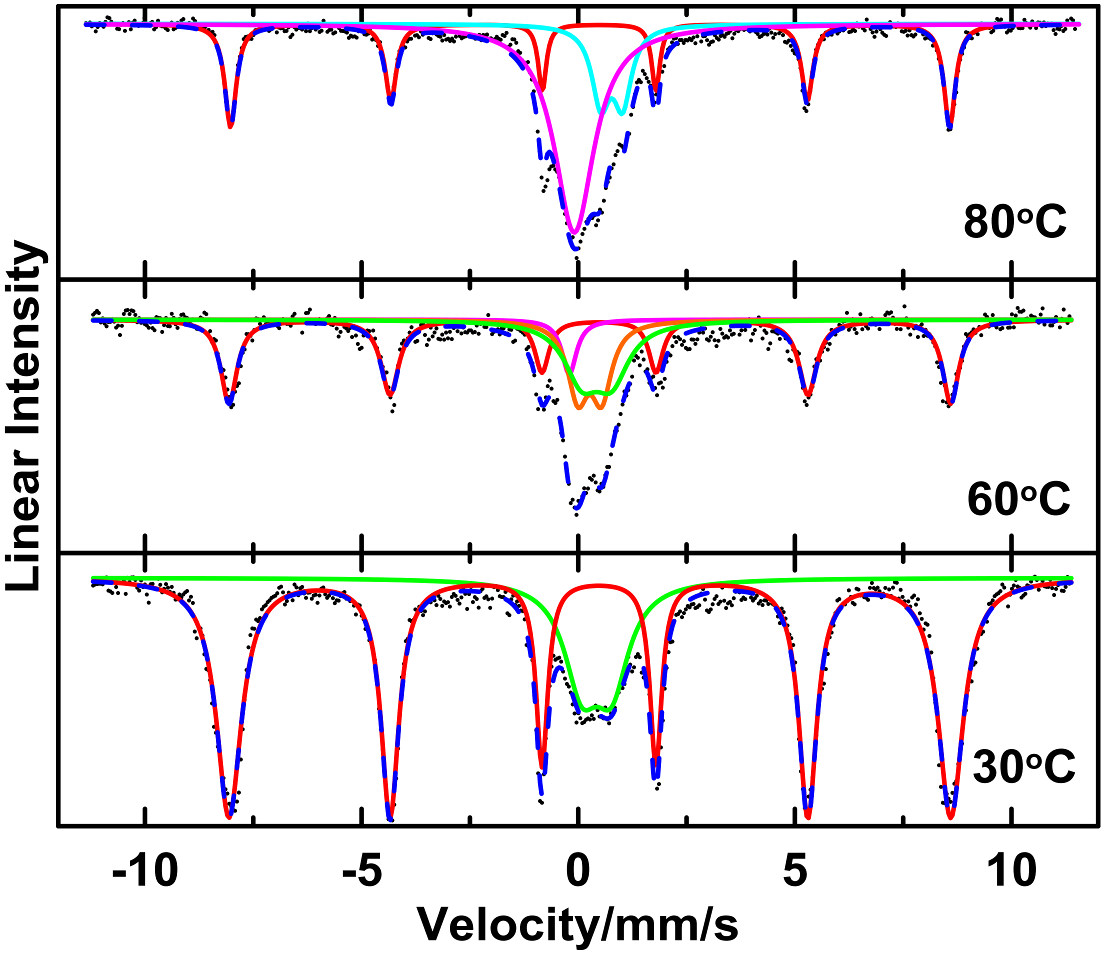

Figure 4.5 Mössbauer spectra for the sodiation of α-Fe_2O_3 at 30°C, 60°C, and 80°C.

The fraction of theoretical capacity of α-Fe_2O_3 observed in Mössbauer spectra (Fig. 4.5) and corresponding specific capacities (accounting for SC/PI) are compared in Figure 4.6. Generally, as the temperature is increased, the capacities deviate from α-Fe_2O_3 consumption observed in the Mössbauer spectra and the standard deviation of capacities also increase. These observations are expected, due to the acceleration of electrolyte decomposition at higher temperatures. Again, it is apparent that the electrolyte decomposition at 80°C is quite significant. Sodiation at 80°C is not worth further exploration with the electrolyte used here, and a more suitable electrolyte is needed for higher temperature studies in the future.

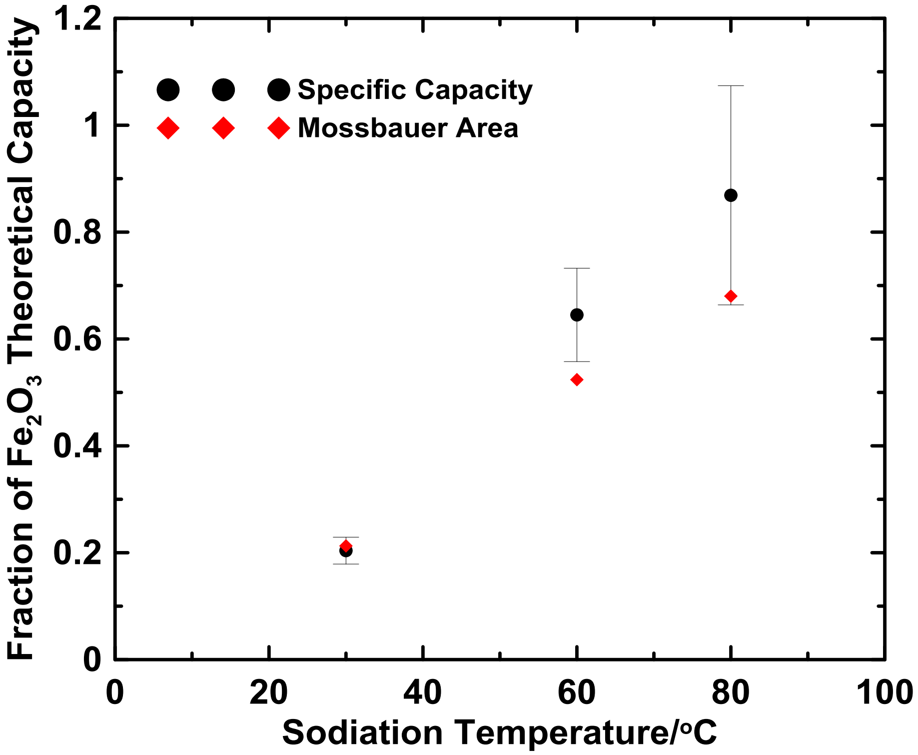

Figure 4.6 Fraction of α-Fe_2O_3 theoretical capacity plotted for specific capacities and Mössbauer spectra for the sodiation of α-Fe_2O_3 at 30°C, 60°C, and 80°C.

The materials resulting from sodiations at 30°C and 60°C were also characterized with X-ray diffraction, shown in Figure 4.7. An XRD pattern was also collected for the empty sample holder. The sample holder has features that overlap with Fe^0, making it difficult to confidently identify any Fe^0 peaks. It is clear that more α-Fe_2O_3 is consumed after one sodiation at 60°C compared to one sodiation at 30°C. The features in XRD patterns due to reaction products are not observed, suggesting the products are either amorphous or the crystallite size is too small to observe by XRD. This observation agrees with the observation of superparamagnetic α-Fe_2O_3 in the Mössbauer spectrum for 30°C sodiation. From the electrochemical and structural characterization, it can be concluded that the increase in capacity at 60°C is not solely due to electrolyte decomposition; an increase in the activity of the conversion reaction of α-Fe_2O_3 with sodium at this higher temperature is observed.

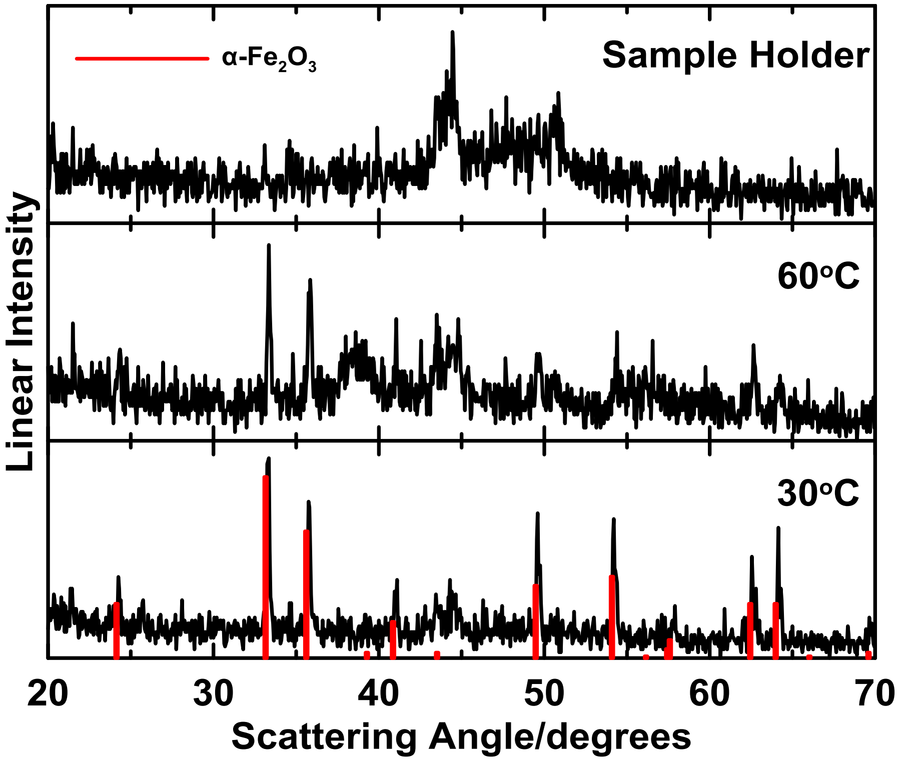

Figure 4.7 XRD patterns for the sodiation of α-Fe_2O_3 at 30°C and 60°C as well as the empty sample holder.

In order to attempt to take advantage of the increased capacity at 60°C, α-Fe_2O_3 electrodes were sodiated once at 60°C, then cycled at 30°C. Cells were either simply cooled to 30°C and cycled (i.e. kept in the "same cell"), or the sodiated electrode was removed under inert atmosphere and placed in a cell with fresh electrolyte and a fresh sodium metal electrode for cycling at 30°C (i.e. placed in a "fresh cell"). The voltage curves for these types of cells are shown in Figure 4.8. The voltage curve for the same cell fades significantly at both discharge and charge endpoints, whereas the fresh cell fades significantly only at charge endpoints. It appears the fresh electrolyte and fresh sodium are beneficial for cycling performance. In other words, high temperature sodiations are detrimental to electrolyte and/or sodium metal cycling performance. This realization lead to adopting the fresh cell procedure for future capacity enhancement attempts by thermal means.

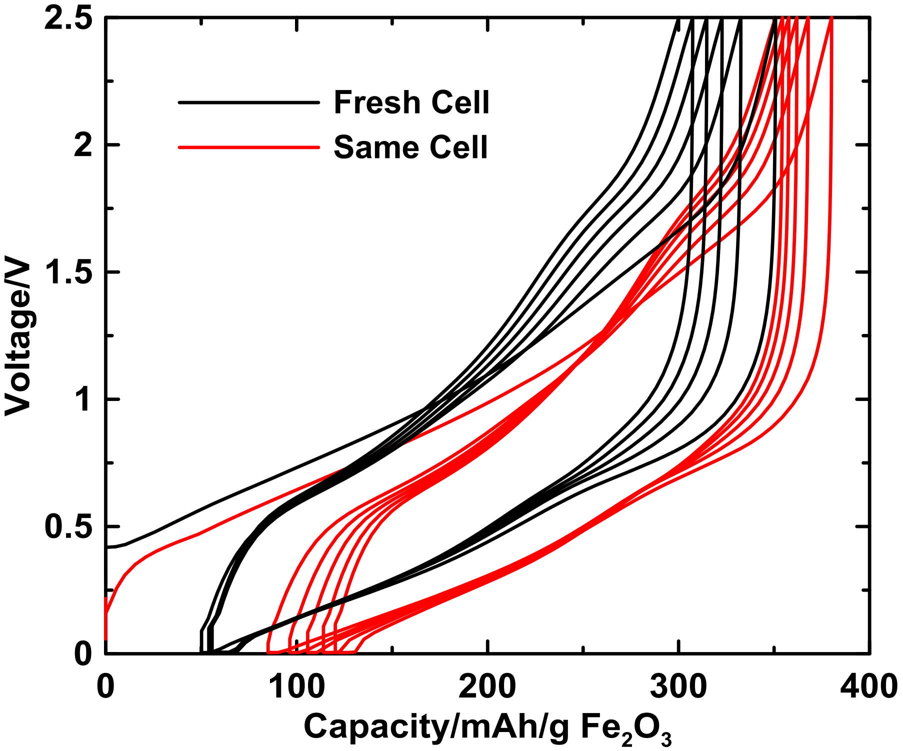

Figure 4.8 The voltage curves for α-Fe_2O_3 electrodes that were sodiated at 60°C followed by cycling at 30°C using "fresh" cell and "same" cell procedures.

The cycling performance of α-Fe_2O_3 electrodes sodiated at 60°C and placed in fresh cells for 30°C cycling are compared to 60°C and 30°C cells in Figure 4.9. The fade of the fresh cells was improved compared to the 60°C cells. However, the capacity of the fresh cells dropped below the capacity of the standard 30°C cells quickly, partly due to the increasing nature of the capacity for standard 30°C cells. As suggested previously, the capacity increase is likely due to a combination of electrolyte decomposition as well as activating new α-Fe_2O_3 through electrochemical grinding. Only about 40% of the theoretical capacity α-Fe_2O_3 electrodes at 30°C is reached at peak capacity. It appears a complex mechanism is occurring, which is discussed further below.

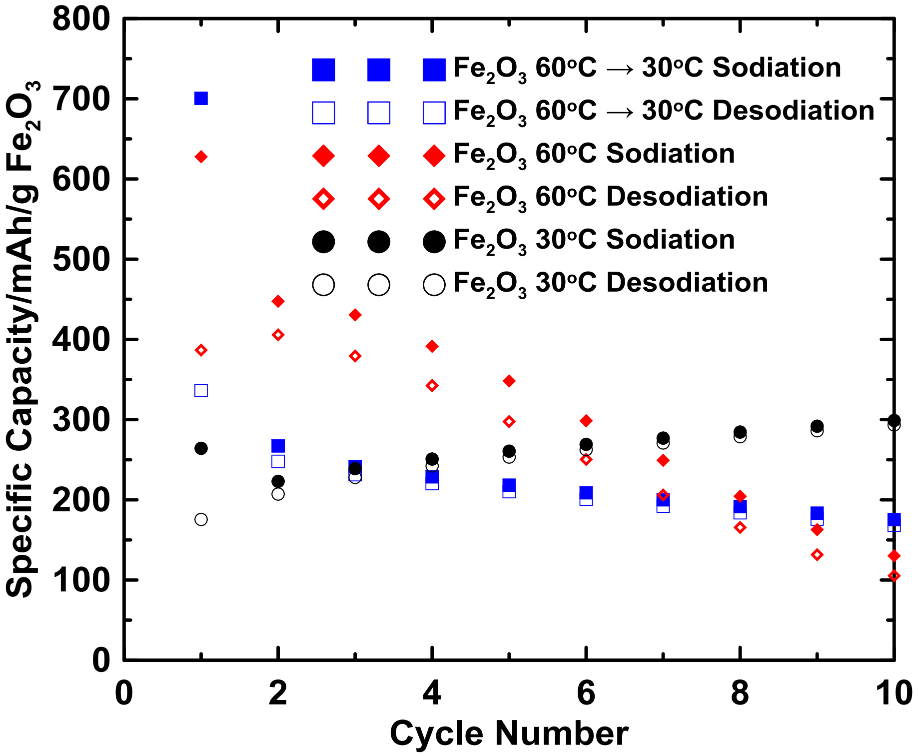

Figure 4.9 Cycling performance of α-Fe_2O_3 electrodes sodiated at 60°C and placed in fresh cells at 30°C, and typical 60°C and 30°C α-Fe_2O_3 cells.

It can be speculated at 30°C, more α-Fe_2O_3 is being activated every cycle, while simultaneously some is being disconnected; and fade commences when the supply of α-Fe_2O_3 becomes depleted (which occurred around 30 cycles for the α-Fe_2O_3 electrodes coated on copper). At 80°C there is more α-Fe_2O_3 activated initially, however excessive electrolyte decomposition products and disconnection of α-Fe_2O_3 might cause excessive fade. The 60°C sodiation increases the consumption of α-Fe_2O_3 such that the majority of the α-Fe_2O_3 has been activated. With activation, there is simultaneous acceleration of electrolyte decomposition and disconnection of α-Fe_2O_3. This mechanism can describe the immediate fade observed for fresh cells at 30°C. In order words, the 60°C sodiation accelerates the α-Fe_2O_3 reaction such that its behavior at the first cycle at 30°C is similar to the behavior of a standard 30°C α-Fe_2O_3 cell at 30°C after it has reached peak capacity. Overall, high temperature sodiations of α-Fe_2O_3 do not appear to improve the performance of the standard 30°C α-Fe_2O_3 cells when using the electrolyte this study. However, an increase in activity of the original conversion reaction by increase in temperature was observed which can be useful.

4.4 ELECTROCHEMICAL ACTIVATION OF CoO

Despite minimal success with enhancing the electrochemical performance of α-Fe_2O_3 via high temperature sodiation it was of interest to pursue a material that exhibits negligible electrochemical activity with sodium at room temperature using this method, since an increase in activity of the conversion reaction of α-Fe_2O_3 was observed at elevated temperatures. As mentioned previously, CoO is thought to be electrochemically inactive with sodium, based on room temperature experiments.[70] However, the full reduction to Co^0 by sodium has a favorable Gibbs free energy of reaction.[29] Therefore, the conversion reaction of sodium with CoO must be kinetically limited. High temperature sodiations may improve the kinetics such that CoO is active at room temperature.

The first three cycles for the voltage curve of a CoO/SC/PI cell is shown in Figure 4.10. Including the contribution from SC/PI, the electrode only has ~80 mAh/g reversible capacity or 9% of theoretical reversible capacity. As observed with α-Fe_2O_3, the voltage curve of CoO also has charge and discharge endpoint slippage towards higher capacity values which suggests electrolyte decomposition is occurring. Overall there is minimal electrochemical activity of CoO with sodium which agrees with previous reports. At

60°C, while larger initial capacities are realized, the capacity fades quickly. Again, this could be due to accelerated electrolyte decomposition and/or particle disconnection upon sodiation/desodiation.

From the work with α-Fe_2O_3 discussed above, 60°C was chosen for high temperature sodiation trials using the fresh cell procedure. Electrolyte decomposition was not as pronounced at this temperature and it was clear that the activity of the α-Fe_2O_3 conversion reaction was increased. Figure 4.11 shows the first three cycles for CoO at 30°C after one sodiation at 60°C. The capacity was significantly increased for CoO compared to its original cycling behavior at 30°C. Slippage of the discharge endpoint appears to have decreased considerably as well. However, the voltage hysteresis was large which is common for conversion reactions.

The cycling performance of CoO electrodes sodiated at 60°C and placed in fresh cells for 30°C cycling are compared to standard 30°C cells in Figure 4.12. The contribution from SC/PI has been subtracted from these capacities. As mentioned above, the cell at 60°C exhibited poor cycling performance, having no observable capacity after 10 cycles. The capacity was larger for fresh cells that were initially sodiated at 60°C, for over 10 cycles. This suggests high temperature sodiation successfully activated CoO cells for room temperature electrochemistry. However, the typical fade associated with conversion mechanisms is apparent and the benefits of high temperature sodiation are not significant after 10 cycles. The same mechanism proposed for α-Fe_2O_3 is suspected for CoO, where the fade corresponds to excessive electrolyte decomposition at the electrode surface and particle disconnection upon activation of CoO. This is one method to activate

CoO with sodium. With electrode optimization and an appropriate electrolyte these benefits may be sustained over more cycles.

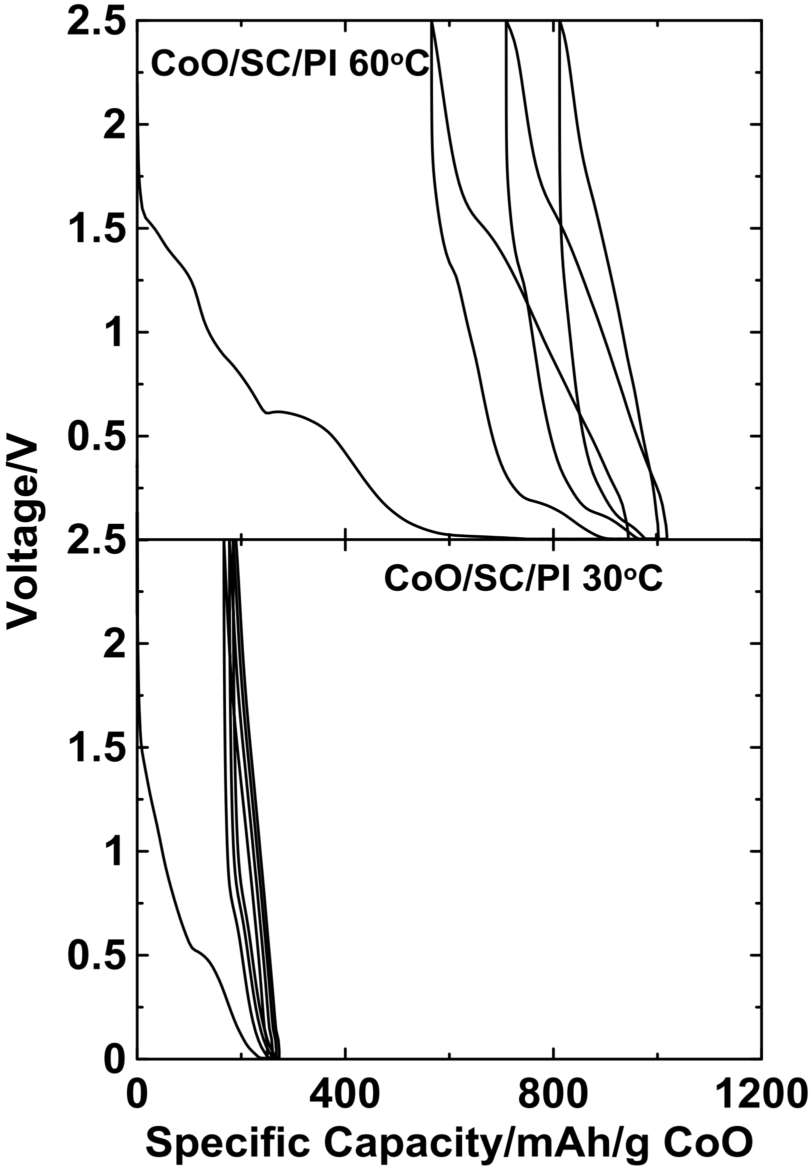

Figure 4.10 Voltage curve for the first three cycles of CoO/SC/PI electrodes at C/25 with a trickle to C/50 in sodium half cells at 30°C and 60°C.

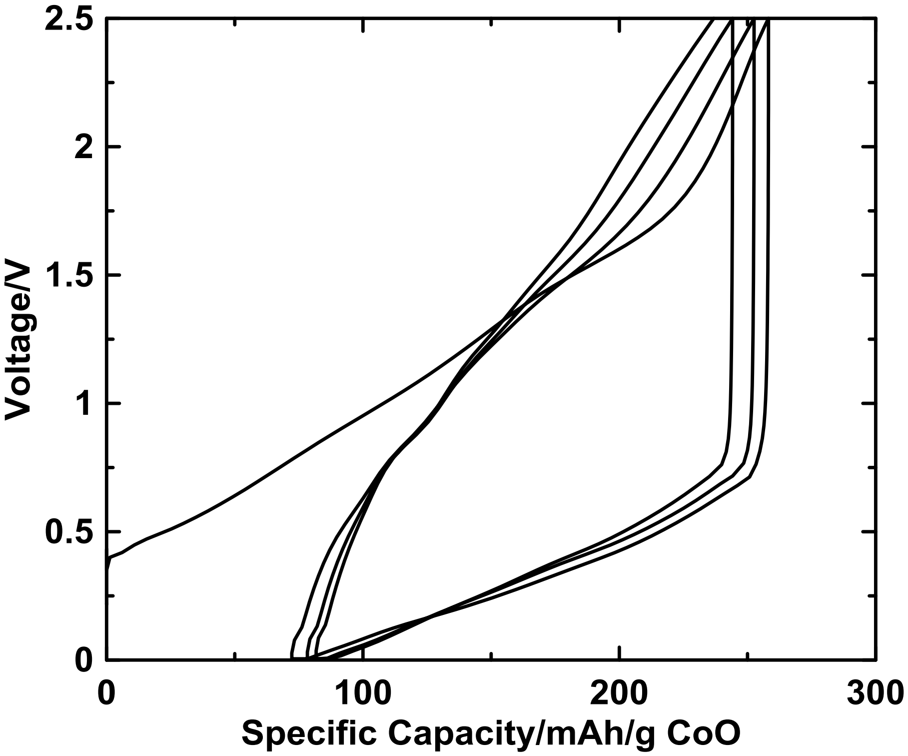

Figure 4.11 Voltage curve for the first three cycles of CoO/SC/PI electrodes at C/25 with a trickle to C/50 in sodium half cells at 30°C after one 60°C sodiation.

Reducing crystallite size of binary metal compounds via ball milling with conductive additive has proven to be successful in improving the kinetics such that cycling performance with lithium is enhanced.[59] It was therefore of interest to couple high temperature sodiation with ball milling of materials in order to determine if there is synergy between the two. CoO was ball milled with SC as described above. The XRD patterns of initial CoO powder, ball milled CoO/SC and cured (CoO/SC)/PI electrodes (as described in Chapter 2) are shown in Figure 4.13. The CoO peaks were broadened by ball milling, indicating a reduction in crystallite size. The average dimension of the crystallites was estimated to be about 15 nm by the CoO [200] peak using the Scherrer equation. After fabricating and curing electrodes, no change was observed in the XRD pattern indicating the CoO material was not modified by the electrode fabrication process.

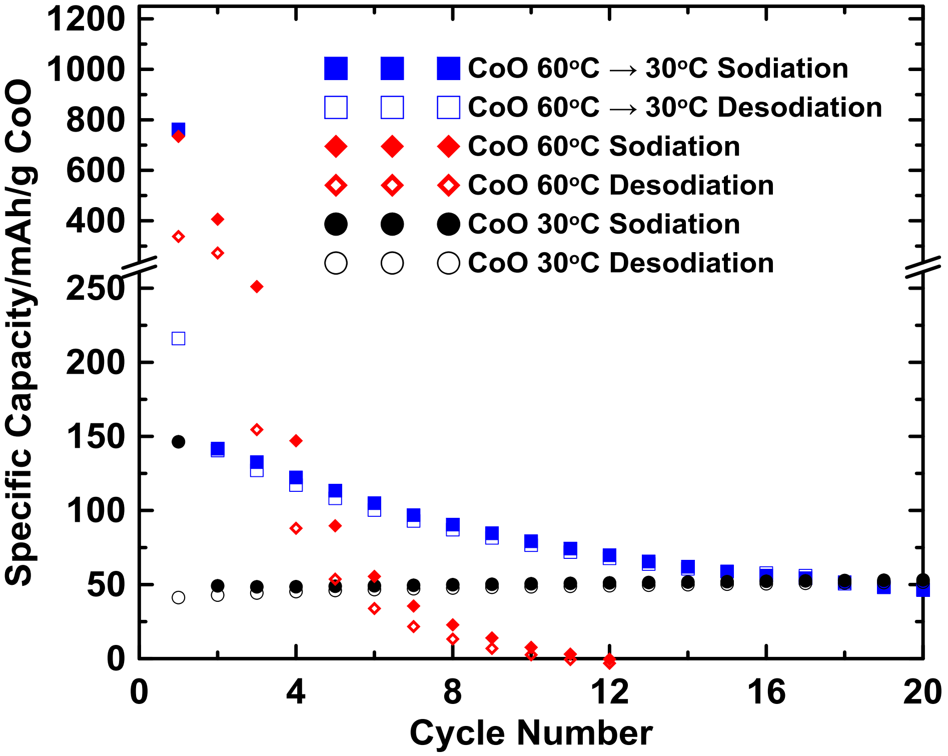

Figure 4.12 Cycling performance of CoO electrodes sodiated at 60°C and placed in fresh cells at 30°C, and typical 30°C CoO cells.

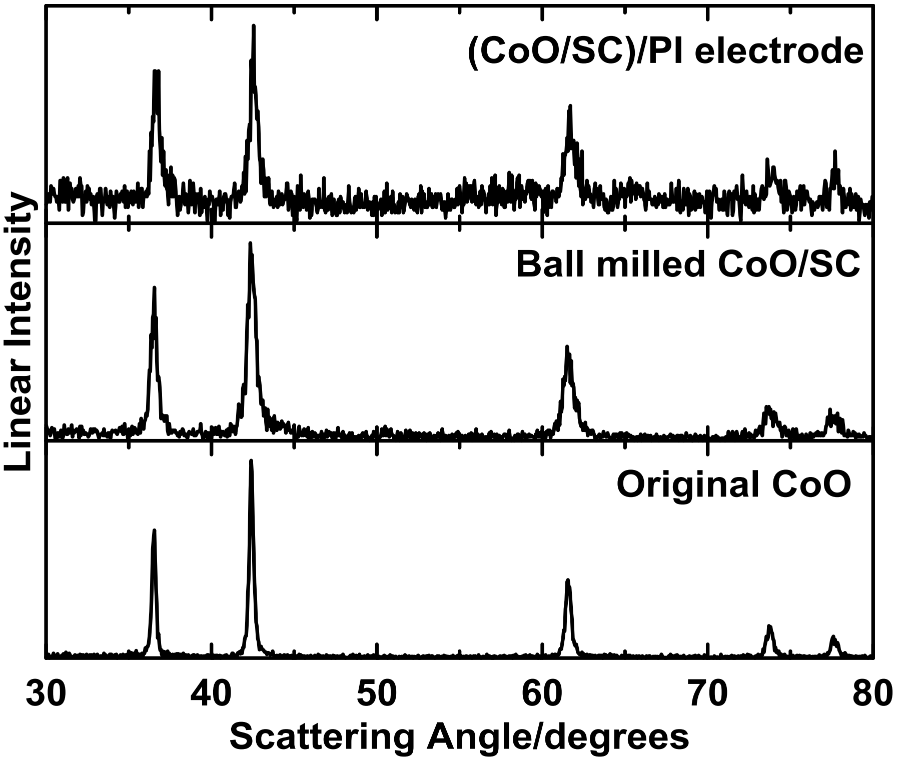

Figure 4.13 The XRD patterns of initial CoO powder, ball milled (CoO/SC) and cured (CoO/SC)/PI electrodes.

The voltage curve for the first three cycles of (CoO/SC)/PI sodium half-cells at 30°C and 60°C are shown in Figure 4.14. Ball milled CoO had significant reversible capacity of 200 mAh g^{-1} at 30°C. It appears ball milling CoO with SC is another method to activate CoO for room temperature electrochemistry with sodium. At 60°C, the reversible capacity was more than 100 mAh/g higher, but the amount of voltage curve slippage was also significant. This suggests more CoO might be accessed with high temperature sodiation but excessive electrolyte decomposition and particle disconnection are present.

Figure 4.15 shows the XRD patterns for (CoO/SC)/PI electrodes sodiated at 30°C and 60°C as well as the pattern for the empty sample holder. As in the α-Fe_2O_3 case, the products from the conversion reaction of CoO with sodium are either amorphous or the crystallite size is too small to observe any diffraction. Comparing the patterns for 30°C and 60°C, more CoO is consumed at the higher temperature, with a nearly featureless XRD pattern. This suggests that the higher temperature does indeed increase activity of the conversion reaction, and extra capacity is not solely associated with electrolyte decomposition. Voltage hysteresis remained large at the higher temperature, as observed with α-Fe_2O_3.

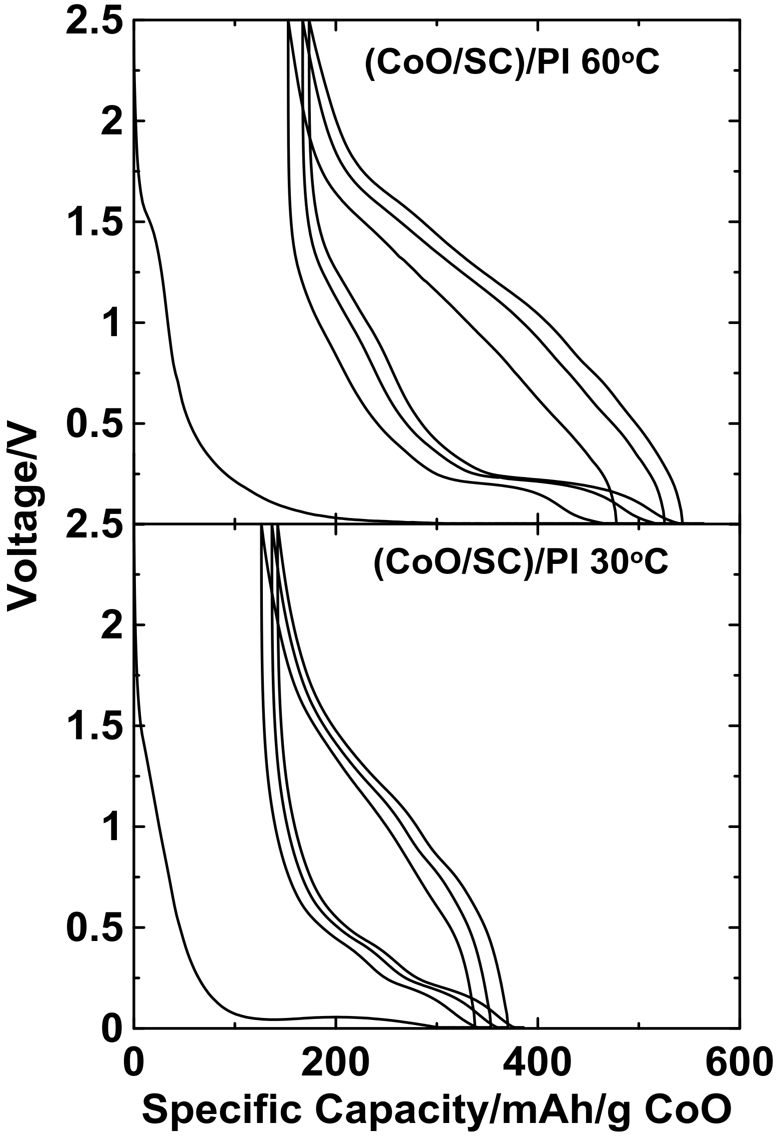

Figure 4.14 Voltage curve for the first three cycles of (CoO/SC)/PI electrodes at C/60 with a trickle to C/120 in sodium half cells at 30°C (bottom) and 60°C (top).

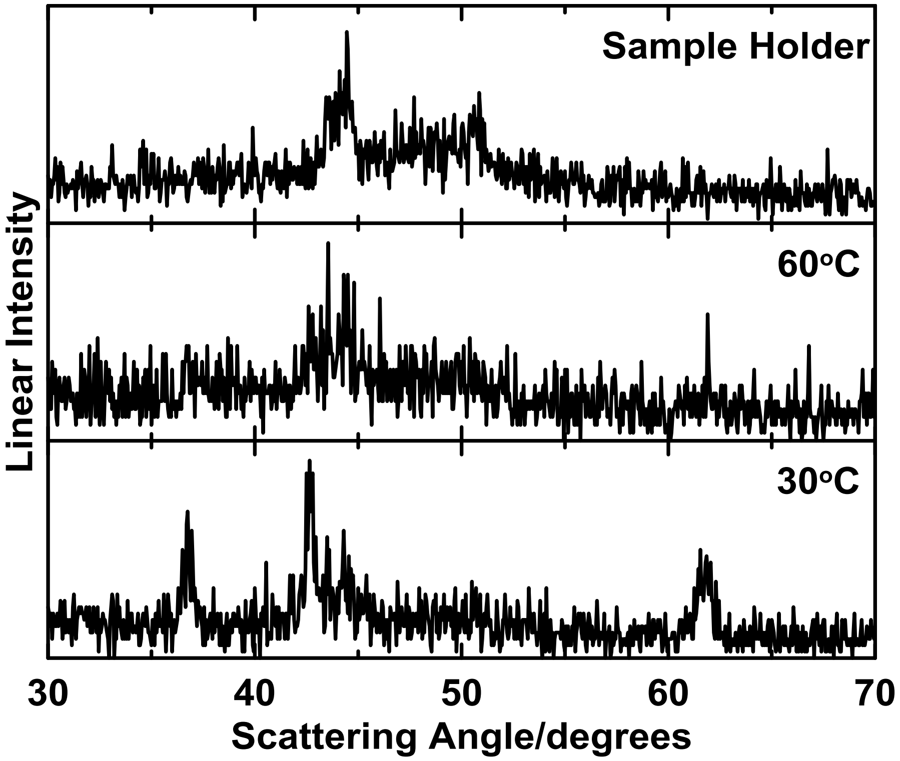

Figure 4.15 XRD patterns for the sodiation of (CoO/SC)/PI at 30°C and 60°C as well as the empty sample holder.

The voltage curve for the first three cycles of (CoO/SC)/PI electrodes sodiated at 60°C and cycled at 30°C in fresh cells is shown in Figure 4.16. Both the hysteresis and voltage curve slippage were significantly reduced compared to previous samples. The cycling performance of CoO electrodes sodiated at 60°C and placed in fresh cells for 30°C cycling are compared to 60°C and 30°C cells in Figure 4.17. Note that the SC/PI contribution is not subtracted as the TiN/SC/PI electrodes are not similar enough compared to the (CoO/SC)/PI electrodes. For the fresh cells cycled at 30°C, there were some capacity benefits for the first cycles compared to a standard 30°C cell, but the standard 30°C cell increases in capacity during cycling, eventually exceeding the capacity of the thermally activated cell.

The cycling behavior of both room temperature CoO and α-Fe_2O_3 were similar. Cycling behavior is also similar for room temperature conversion reactions of binary oxides with lithium.[55] As in the Fe_2O_3 case, the full theoretical capacity was not observed for any CoO cell. As suggested previously, this could be due to simultaneous particle disconnection and material activation during cycling. The cycling performance was significantly improved for the (CoO/SC)/PI electrodes that were thermally activated, with a large volumetric energy density of 1800 Ah/L from 0 to 2.5 V. It appears that at least short term cycling performance is enhanced with high temperature sodiation. This cycling performance might be due to CoO being consumed at the same rate it is being activated, explaining why there is no increasing capacity behavior. Reducing crystallite size improves the kinetics such that more capacity can be accessed. Therefore, by coupling high temperature discharge and optimizing crystallite size, an electrochemically inactive material can be given a chance for use in metal ion battery chemistry at room temperature.

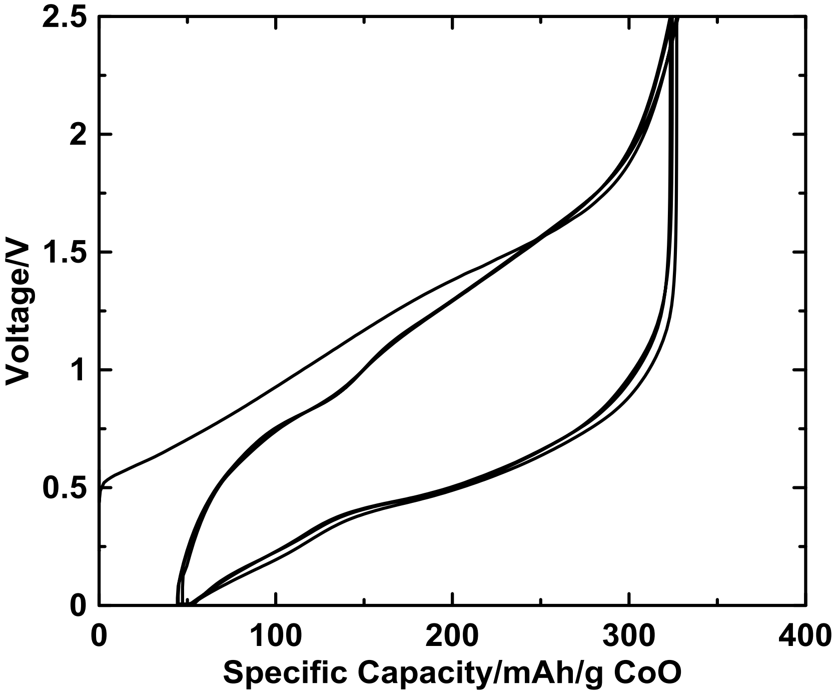

Figure 4.16 Voltage curve for the first three cycles of (CoO/SC)/PI electrodes at C/60 with a trickle to C/120 in sodium half cells at 30°C after one 60°C sodiation.

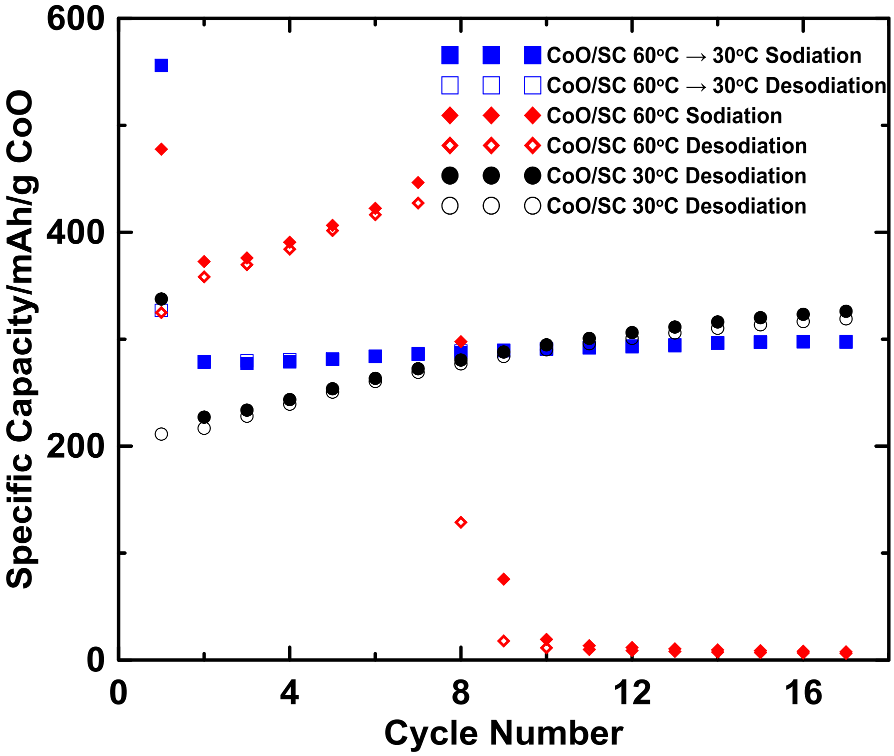

Figure 4.17 Cycling performance of (CoO/SC)/PI electrodes sodiated at 60°C and placed in fresh cells at 30°C, and standard 60°C and 30°C (CoO/SP)/PI cells.

4.5 CONCLUSION

The effects of elevated temperature electrochemistry of binary transition metal oxides were explored. Using α-Fe_2O_3 as a case study, an increase in temperature was observed to increase activity of conversion reactions. α-Fe_2O_3 cells at temperatures exceeding 80°C did not cycle, likely to due to increased electrolyte decomposition and particle disconnection. Cells sodiated at 60°C were able to cycle at room temperature, with typical fade associated with conversion reactions. It appears that high temperature sodiation does not benefit an already room temperature active material. Although a stable electrolyte and optimized electrode design may allow for room temperature access of increased capacity that is present at higher temperature.

Two methods for activating room temperature inactive CoO with sodium were shown. Activating CoO with high temperature sodiation leads to significant increase in specific capacity, but poor cycling performance and large voltage hysteresis. Activating CoO by ball milling with carbon black also leads to significant increase in specific capacity. These electrodes had improved cycling performance compared to high temperature activation. Voltage hysteresis was not improved in any case, which agrees with in previous reports for the lithiation of conversion materials at elevated temperatures. Coupling the two activation methods results in significantly improved cycling performance relative to the separate methods and achieved a volumetric capacity of 1800 Ah/L from 0 to 2.5 V. These methods can be applied to other reactions in metal ion battery chemistry that have a spontaneous Gibbs free energy of reaction at room temperature. With improvement of electrode design and electrolyte, more materials that initially appear inactive at room temperature, but have a spontaneous Gibbs free energy of reaction, might be activated by thermal means and/or particle size reduction.

CHAPTER 5 CONCLUSION

5.1 CONCLUSION AND FUTURE WORK

A crucial limitation for realization of commercial sodium-ion batteries is the lack of suitable negative electrode materials. Common negative electrode materials like hard carbon do not have the energy density to compete with its lithium ion battery counterpart, graphite.[20] Metal oxides that undergo intercalation reactions are promising, but are limited by the finite number of vacancies for sodium ions.[26] Alloy materials are also promising due to their significantly large reversible capacity, but characteristics intrinsic to the alloying reaction, e.g. large volume expansion, limit their development.[14] Materials undergoing conversion reactions may be another option for creating high energy density negative electrode materials.

Conversion reactions are relatively new to sodium-ion battery technology and hence have several issues to overcome. These issues include large voltage hysteresis, low coulombic efficiency and large capacity fade. Unique materials were explored in this thesis in an attempt to increase energy density and reduce energy efficiency penalties of negative electrode materials for sodium-ion battery technology. These materials are also applicable to lithium ion battery technology. A survey of mixed transition metal titanates and vanadate materials for use as negative electrodes in Na-ion cells was conducted because of the low voltage redox couples of $Ti^{3+/4+}$ and $V^{2+/3+}$. Some of these materials were observed to undergo mechanisms atypical to conversion reactions. Although the reversible sodiation capacities are generally much smaller than that of Li, the volumetric sodiation capacities for some of the compounds surveyed were nevertheless quite high. In fact MnV_2O_6, CoV_3O_8, and $VFeO_4$ (820 - 1163 Ah/L) all have reversible volumetric capacities that far exceed that of hard carbon (~450 Ah/L) and even that of graphite in a lithium ion cell (~730 Ah/L). $Ca_5Co_4(VO_4)_6$ and $CoTiO_3$ were other notable materials with volumetric capacities of 625 Ah/L and 692 Ah/L, respectively. It is also worth noting this is the first known report of the lithiation of $Ca_5Co_4(VO_4)_6$, which had a measured volumetric capacity of 2414 Ah/L. However, most of these materials exhibited undesirable voltage hysteresis and poor cycling performance, with the latter being expected given that neither the electrode fabrication nor electrolyte formulation were optimized.

$CoTiO_3$ was found to have particularly interesting characteristics as an anode in sodium cells. After 30 cycles the voltage curve hysteresis of $CoTiO_3$ reduced to only 440 mV. The volume expansion during sodiation was measured to be only 6%. Both the low hysteresis and low volume expansion are suggestive of an intercalation type mechanism. If such oxides could be made with low irreversible capacity they would be attractive for use as high volumetric capacity anodes in sodium-ion cells.

Due to the large reversible capacity for binary metal oxides in lithium-ion technology, it was also of interest to explore their application in sodium-ion battery technology. Furthermore, the electrochemistry of these oxides with sodium at elevated temperatures were explored. Using α-Fe_2O_3 as a case study, an increase in temperature was observed to increase the activity of conversion reactions. α-Fe_2O_3 cells at temperatures exceeding 80°C did not cycle, likely to due to increased electrolyte decomposition and particle disconnection. Cells sodiated at 60°C were able to cycle at room temperature, with typical capacity fade associated with conversion reactions. It appears that high temperature sodiation does not benefit an already room temperature active material. However, a stable electrolyte and optimized electrode design may allow for room temperature access of increased capacity that is present at higher temperature.

The same methods used to cycle α-Fe_2O_3 at elevated temperatures were applied to the claimed inactive CoO with sodium. Activating CoO with high temperature sodiation leads to significant increase in specific capacity, but poor cycling performance and large voltage hysteresis are apparent. Activating CoO by ball milling with carbon black also leads to significant increase in specific capacity. This ball milled CoO had improved cycling performance compared to high temperature activation. Coupling the activation methods results in significantly improved cycling performance relative to the two separate methods. The originally room temperature inactive CoO was shown to cycle with a large volumetric capacity of 1800 Ah/L from 0 to 2.5 V, which is over double the volumetric capacity of graphite versus lithium. These methods can be applied other materials which are inactive at room temperature in metal-ion battery chemistry. With improvement of electrode design and electrolyte, materials that were originally thought to be inactive may be activated by thermal means and/or particle size reduction.

In general, electrochemical mechanisms for these metal oxides need to be investigated in greater detail. Given that virtually all of these materials decompose to an amorphous structure upon sodiation, XRD is not enough to understand their chemistry. Mössbauer spectroscopy was useful for structural characterization but unfortunately Mössbauer spectroscopy is limited to only Fe-containing materials in this work. Characterization techniques such as X-ray photoelectron spectroscopy, extended X-ray absorption fine structure spectroscopy, and nuclear magnetic resonance spectroscopy may be more informative for exploring the amorphous chemistry of these materials with sodium. Structural investigations of these materials are necessary in order to further develop their electrochemical performance.

5.2 OUTLOOK FOR SODIUM-ION CONVERSION NEGATIVE ELECTRODES

The future for sodium-ion conversion materials is unknown. In this thesis, several materials were explored, with many showing appreciable specific and volumetric capacities. Cycling performance is typically poor, but might be improved with appropriate electrode design and electrolyte optimization. Further, the reactivity of electrolyte with conversion materials is an important safety issue that needs to be investigated. Even if these problems were solved, the large voltage hysteresis for these conversion materials still limits their commercial realization. There may be some insight already for how to solve this hysteresis issue with the low hysteresis $CoTiO_3$ material described in Chapter 3 as well as the conversion cathode, $Cu_yFe_{1-y}F_2$, mentioned in Chapter 4. Hopefully the activation methods explored in this thesis will help accelerate discovery of overlooked materials and give rise to materials with practical properties. Overall, conversion negative electrodes for sodium-ion batteries have significant challenges to overcome if they are ever to become commercially viable.

References

1. C. Potvin, S. Aitken, F. Anctil, E. Bennett, F. Berkes, J. Byrne, I. Creed, A. Cunsolo Willox, A. Dale, D. de Lange, M. Entz, L. Fraser, G. Hoberg, M. Holden, A. Jacob, S. Jodoin, L. Margolis, J. Meadowcroft, C. Morency, N. Mousseau, K. Oakes, S. Otto, T. S. Palmer, D. Paquin, A. Perl, A. Potvin, C. Raudsepp-Hearne, B. Sinclair, N. Slawinski, M. Stoddart, and T. Wright, *Acting On Climate Change: Solutions From Canadian Scholars*, p. 1-56, (2015).

2. 2014 Fall Report of the Commissioner of the Environment and Sustainable Development, http://www.oag-bvg.gc.ca/internet/English/att__e_39876.html (accessed May 16, 2015).

3. National Inventory Report 1990-2013: Greenhouse Gas Sources and Sinks in Canada - Executive Summary, http://www.ec.gc.ca/ges-ghg/default.asp?lang=En&n=5B59470C-1&offset=3&toc=show#table_S2 (accessed May 20, 2015).

4. G. Wu, A. Inderbitzin, and C. Bening, *Energy Policy*, **80**, 196 (2015).

5. J. Dumortier, S. Siddiki, S. Carley, J. Cisney, R. M. Krause, B. W. Lane, J. A. Rupp, and J. D. Graham, *Transp. Res. Part A*, **72**, 71 (2015).

6. D. Andre, S.-J. Kim, P. Lamp, S. F. Lux, F. Maglia, O. Paschos, and B. Stiaszny, *J. Mater. Chem. A*, **3**, 6709 (2015).

7. M. M. Thackeray, C. Wolverton, and E. D. Isaacs, *Energy Environ. Sci.*, **5**, 7854 (2012).

8. http://www.teslamotors.com/blog/2013-model-s-price-increase (accessed July 22, 2015).

9. DoE Annual Merit Review 2012, http://www.annualmeritreview.energy.gov/ (accessed May 16, 2015).

10. M. W. Gaultois, T. D. Sparks, C. K. H. Borg, R. Seshadri, W. D. Boni, and D. R. Clarke, *Chem. Mater.*, **25**, 2911 (2013).

11. U.S. Department of Justice and the Federal Trade Commission. Horizontal merger guidelines; 2010. http://www.justice.gov/atr/public/guidelines/hmg-2010.html (accessed May 21, 2015).

12. http://www.mrl.ucsb.edu:8080/datamine/thermoelectrics.jsp (accessed May 21, 2015).

13. B. M. L. Rao, R. W. Francis, and H. A. Christopher, *J. Electrochem. Soc.*, **124**, 1490 (1977).

14. M. Dahbi, N. Yabuuchi, K. Kubota, K. Tokiwa, and S. Komaba, *Phys. Chem. Chem. Phys.*, **16**, 15007 (2014).

15. R. D. Shannon, *Acta Crystallogr. Sect. A*, **32**, 751 (1976).

16. D. Kundu, E. Talaie, V. Duffort, and L. F. Nazar, *Angew. Chemie Int. Ed.*, **54**, 3431 (2015).

17. N. Yabuuchi, K. Kubota, M. Dahbi, and S. Komaba, *Chem. Rev.*, **114**, 11636 (2014).

18. D. Linden and T. B. Reddy, Eds., Linden?s Handbook of Batteries, 4th ed., McGrawHill, (2010).

19. D. P. DiVincenzo and E. J. Mele, *Phys. Rev. B*, **32**, 2538 (1985).

20. D. A. Stevens and J. R. Dahn, *J. Electrochem. Soc.*, **147**, 1271 (2000).

21. L. D. Ellis, T. D. Hatchard, and M. N. Obrovac, *J. Electrochem. Soc.*, **159**, A1801 (2012).

22. J. Qian, Y. Chen, L. Wu, Y. Cao, X. Ai, and H. Yang, *Chem. Commun. (Camb).*, **48**, 7070 (2012).

23. N. Yabuuchi, Y. Matsuura, T. Ishikawa, S. Kuze, J.-Y. Son, Y.-T. Cui, H. Oji, and S. Komaba, *ChemElectroChem*, **1**, 580 (2014).

24. P. Senguttuvan, M. R. Palacín, G. Rousse, V. Seznec, and J.-M. Tarascon, *Chem. Mater.*, **23**, 4109 (2011).

25. R. Shanmugam and W. Lai, *ECS Electrochem. Lett.*, **3**, A23 (2014).

26. R. Fielden and M. N. Obrovac, *J. Electrochem. Soc.*, **161**, A1158 (2014).

27. Y. Xu, E. M. Lotfabad, H. Wang, B. Farbod, Z. Xu, A. Kohandehghan, and D. Mitlin, *Chem. Commun. (Camb).*, **49**, 8973 (2013).

28. R. Malini, U. Uma, T. Sheela, M. Ganesan, and N. G. Renganathan, *Ionics (Kiel).*, **15**, 301 (2008).

29. F. Klein, B. Jache, A. Bhide, and P. Adelhelm, *Phys. Chem. Chem. Phys.*, **15**, 15876 (2013).

30. J. Cabana, L. Monconduit, D. Larcher, and M. R. Palacín, *Adv. Mater.*, **22**, 170 (2010).

31. Y. Jiang, M. Hu, D. Zhang, T. Yuan, W. Sun, B. Xu, and M. Yan, *Nano Energy*, **5**, 60 (2014).

32. R. Alcantara, M. Jaraba, P. Lavela, and J. L. Tirado, *Chem. Mater.*, **14**, 2847 (2002).

33. M. C. López, P. Lavela, G. F. Ortiz, and J. L. Tirado, *Electrochem. Commun.*, **27**, 152 (2013).

34. M. V Reddy, G. V. S. Rao, and B. V. R. Chowdari, *Chem. Rev.*, **113**, 5364 (2013).

35. A. Ponrouch, J. Cabana, R. Dugas, J. L. Slack, and M. R. Palacín, *RSC Adv.*, **4**, 35988 (2014).

36. F. Wang, S. Kim, D. Seo, K. Kang, L. Wang, D. Su, J. J. Vajo, J. Wang, and J. Graetz, *Nat. Commun.*, **6**, 1 (2015).

37. B. D. Cullity, Elements of X-Ray Diffraction; 1st ed.; Addison-Wesley Publishing Company Inc.: Reading, Massachusetts, (1956).

38. J. I. Langford and A. J. C. Wilson, *J. Appl. Crystallogr.*, **11**, 102 (1978).

39. N. N. Greenwood, T. C. Gibb, Mossbauer Spectroscopy, Chapman and Hall Ltd., London, Great Britain, (1971).

40. M. D. Dyar, D. G. Agresti, M. W. Schaefer, C. A. Grant, and E. C. Sklute, *Annu. Rev. Earth Planet. Sci.*, **34**, 83 (2006).

41. S. Kim, H. Ikuta, and M. Wakihara, *Solid State Ionics*, **139**, 57 (2001).

42. S. Denis, E. Baudrin, M. Touboul, and J.-M. Tarascon, *J. Electrochem. Soc.*, **144**, 4099 (1997).

43. S. Denis, E. Baudrin, F. Orsini, G. Ouvrard, M. Touboul, and J.-M. Tarascon, *J. Power Sources*, **81-82**, 79 (1999).

44. S. Denis, R. Dedryve, E. Baudrin, S. Laruelle, M. Touboul, J. C. Jumas, and J. M. Tarascon, *Chem. Mater.*, **144**, 3733 (2000).

45. P. Poizot, E. Baudrin, S. Laruelle, L. Dupont, M. Touboul, and J. M. Tarascon, *Solid State Ionics*, **138**, 31 (2000).

46. P. Poizot, S. Laruelle, S. Grugeon, and J.-M. Tarascon, *J. Electrochem. Soc.*, **149**, A1212 (2002).

47. D. Hara, J. Shirakawa, H. Ikuta, Y. Uchimoto, M. Wakihara, T. Miyanaga, and I. Watanabe, *J. Mater. Chem.*, **12**, 3717 (2002).

48. T. Morishita, H. Konno, Y. Izumi, and M. Inagaki, *Solid State Ionics*, **177**, 1347 (2006).

49. R. Fernández de Luis, A. Ponrouch, M. R. Palacín, M. K. Urtiaga, and M. I. Arriortua, *J. Solid State Chem.*, **212**, 92 (2014).

50. International Centre for Diffraction Data, *PDF-2* (2002).

51. E. Baudrin, S. Laruelle, S. Denis, M. Touboul, and J. Tarascon, *Solid State Ionics*, **123**, 139 (1999).

52. Z. Du, R. A. Dunlap, and M. N. Obrovac, *J. Electrochem. Soc.*, **161**, A1698 (2014).

53. Y. Sun, L. Zhao, H. Pan, X. Lu, L. Gu, Y. Hu, H. Li, M. Armand, Y. Ikuhara, L. Chen, and X. Huang, *Nat. Commun.*, **4**, 1870 (2013).

54. J. Lee, A. Urban, X. Li, D. Su, G. Hautier, and G. Ceder, *Science*, **343**, 519 (2014).

55. P. Poizot, S. Laruelle, S. Grugeon, L. Dupont, and J. M. Tarascon, *Nature*, **407**, 496 (2000).

56. Y. Oumellal, A. Rougier, G. A. Nazri, J.-M. Tarascon, and L. Aymard, *Nat. Mater.*, **7**, 916 (2008).

57. F. Gillot, L. Monconduit, and M. L. Doublet, *Chem. Mater.*, **17**, 5817 (2005).

58. Y. Wang, Z.-W. Fu, X.-L. Yue, and Q.-Z. Qin, *J. Electrochem. Soc.*, **151**, E162 (2004).

59. F. Badway, F. Cosandey, N. Pereira, and G. G. Amatucci, *J. Electrochem. Soc.*, **150**, A1318 (2003).

60. L. Croguennec and M. R. Palacin, *J. Am. Chem. Soc.*, **137**, 3140 (2015).

61. F. Sauvage, J. M. Tarascon, and E. Baudrin, *J. Phys. Chem. B*, **111**, 9624 (2007).

62. S. Laruelle, S. Grugeon, P. Poizot, M. Dollé, L. Dupont, and J.-M. Tarascon, *J. Electrochem. Soc.*, **149**, A627 (2002).

63. A. Ponrouch, P. L. Taberna, P. Simon, and M. R. Palacín, *Electrochim. Acta*, **61**, 13 (2012).

64. G. Gachot, S. Grugeon, M. Armand, S. Pilard, P. Guenot, J. M. Tarascon, and S. Laruelle, *J. Power Sources*, **178**, 409 (2008).

65. X. Li, L. Qiao, D. Li, X. Wang, W. Xie, and D. He, *J. Mater. Chem. A*, **1**, 6400 (2013).

66. A.-L. Dalverny, J.-S. Filhol, and M.-L. Doublet, *J. Mater. Chem.*, **21**, 10134 (2011).

67. J. Y. Kwon, J. H. Ryu, Y. S. Jung, and S. M. Oh, *J. Alloys Compd.*, **509**, 7595 (2011).

68. J. H. Ku, Y. S. Jung, K. T. Lee, C. H. Kim, and S. M. Oh, *J. Electrochem. Soc.*, **156**, A688 (2009).

69. Y. S. Jung, K. T. Lee, J. H. Kim, J. Y. Kwon, and S. M. Oh, *Adv. Funct. Mater.*, **18**, 3010 (2008).

70. S.-W. Kim, D.-H. Seo, X. Ma, G. Ceder, and K. Kang, *Adv. Energy Mater.*, **2**, 710 (2012).

71. I. Kim, P. N. Kumta, and G. E. Blomgren, *Electrochem. Solid-State Lett.*, **3**, 493 (2000).

72. K. E. Gregorczyk, Y. Liu, J. P. Sullivan, and G. W. Rubloff, *ACS Nano*, **7**, 6354 (2013).

73. D. Larcher, D. Bonnin, R. Cortes, I. Rivals, L. Personnaz, and J.-M. Tarascon, *J. Electrochem. Soc.*, **150**, A1643 (2003).

74. B. Philippe, M. Valvo, F. Lindgren, H. Rensmo, and K. Edström, *Chem. Mater.*, **26**, 5028 (2014).